Two type II phosphatidylinositol 4-kinases function sequentially in tubule-mediated cargo delivery from early endosomes to melanosomes

Yueyao Zhu[1,2], Shuixing Li[1,3], Alexa Jaume[1,3], Riddhi Atul Jani[4], Cédric Delevoye[4], Graça Raposo[4], and Michael S. Marks[1,3,5]

[1]Dept. of Pathology & Laboratory Medicine, Children's Hospital of Philadelphia Research Inst., Philadelphia, PA, USA; [2]Dept. of Biology, University of Pennsylvania School of Arts and Sciences, Philadelphia, PA, USA; [3]Dept. of Pathology & Laboratory Medicine and Dept. of Physiology, Perelman School of Medicine, University of Pennsylvania, Philadelphia, PA, USA; [4]Institut Curie, PSL Research University, CNRS, UMR 144, Structure and Membrane Compartments, Paris, 75005, France.

[5]To whom correspondence should be addressed:
Dept. of Pathology & Laboratory Medicine
Children's Hospital of Philadelphia Research Institute
816G Abramson Res. Ctr., 3615 Civic Ctr. Blvd.
Philadelphia, PA 19104
Tel: 215-590-3664
Email: marksm@pennmedicine.upenn.edu

Running Title: PI4KIIα and PI4KIIβ in tubule extension to melanosomes

Keywords: phosphoinositide; pigmentation; recycling endosomes; early endosomes;

Abbreviations: AP-1, adaptor protein-1; AP-3, adaptor protein-3; BLOC, Biogenesis of Lysosome-related Organelles Complex; HPS, Hermansky-Pudlak syndrome(s); IFM, immunofluorescence microscopy; LROs, lysosome-related organelles; NC, non-target control; OCA2, oculocutaneous albinism type 2 protein; P4C, *Legionella pneumophila* P4C-SidC; P4Mx2, tandem repeat of *Legionella pneumophila* SidM PtdIns4P-binding domain, P4M; P4Mx2PI4K, phosphatidylinositol-4-kinase; PtdIns, phosphatidylinositol; PtdIns4P, phosphatidylinositol-4-phosphate; STX13, syntaxin-12/13; TfR, transferrin receptor; TYRP1, tyrosinase-related protein-1; WT, wild-type

SUMMARY

Contents are delivered from early endosomal intermediates to maturing melanosomes through tubular transport carriers. Zhu et al show that two type II phosphatidylinositol kinases, PI4KIIα and PI4KIIβ, sequentially generate phosphatidylinositol-4-phosphate during tubule initiation and elongation for ultimate melanosome content delivery.

ABSTRACT

Melanosomes are pigment cell-specific lysosome-related organelles in which melanin pigments are synthesized and stored. Melanosome maturation requires delivery of melanogenic cargoes via tubular transport carriers that emanate from early endosomes and that require BLOC-1 for their formation. Here we show that phosphatidylinositol-4-phosphate (PtdIns4P) and the type II PtdIns-4-kinases (PI4KIIα and PI4KIIβ) support BLOC-1-dependent tubule formation to regulate melanosome biogenesis. Depletion of PI4KIIα or PI4KIIβ with shRNAs in melanocytes reduced melanin content and misrouted BLOC-1-dependent cargoes to late endosomes/lysosomes. Genetic epistasis, cell fractionation, and quantitative live-cell imaging analyses show that PI4KIIα and PI4KIIβ function sequentially and non-redundantly downstream of BLOC-1 during tubule elongation towards melanosomes by generating local pools of PtdIns4P. The data demonstrate that both type II PtdIns-4-kinases are necessary for efficient BLOC-1-dependent tubule elongation and subsequent melanosome contact and content delivery during melanosome biogenesis. The independent functions of PtdIns-4-kinases in tubule extension are likely downstream of redundant functions in BLOC-1-dependent tubule initiation.

INTRODUCTION

The endolysosomal system is a highly dynamic network of interacting intracellular membrane-bound compartments that plays essential roles in all cells in nutrient uptake, signaling, metabolism, and pathogen life cycle (Huotari and Helenius, 2011; Klumperman and Raposo, 2014). In certain cell types, the endolysosomal system is additionally adapted to create specialized subcellular membrane-bound compartments termed lysosome-related organelles (LROs) for specific physiological functions (Bowman et al., 2019; Delevoye et al., 2019). LROs share common features with conventional lysosomes but possess distinct morphological and functional characteristics that are conferred largely by their content of cell type-specific constituents (Bowman et al., 2019; Delevoye et al., 2019). While each LRO is unique, many LROs share common biogenetic origins and are generated using common pathways. Notably, abnormalities in the biogenesis of several LROs underlie the pathology of the Hermansky–Pudlak syndromes (HPS), a group of multisystem disorders characterized by oculocutaneous albinism, bleeding diathesis, and other variable symptoms due to defective melanosomes in pigment cells, dense granules in platelets, and additional LROs in other cell types (Bowman et al., 2019; De Jesus Rojas and Young, 2020). How the products of the genes that are defective in HPS facilitate LRO biogenesis and how they interface with additional cellular machinery to effect their functions are only beginning to be understood.

The genes that are defective in HPS encode subunits of four obligate protein complexes – adaptor protein-3 (AP-3) and biogenesis of lysosome-related organelles complex (BLOC)-1, -2 and -3 – that regulate membrane dynamics essential for the biosynthetic delivery of components to maturing LROs and/or recycling of material from LROs (Bowman et al., 2019; Di Pietro and Dell'Angelica, 2005). Much of our understanding of BLOCs and AP-3 function in LRO biogenesis comes from analyses of melanosome maturation in epidermal melanocytes (Le et al., 2021). Melanosomes mature from nonpigmented stage I and II precursors to pigmented organelles by

the delivery of melanogenic enzymes and transporters (Novikoff et al., 1968; Raposo et al., 2001; Seiji et al., 1961). Cargo delivery to maturing melanosomes occurs via three district pathways: one from the Golgi (Patwardhan et al., 2017) and two from distinct early endosomal domains, the latter two regulated by the HPS complexes (Bowman et al., 2019). In particular, one pathway uniquely requires BLOC-1 to generate recycling-endosome-like tubular transport intermediates from sorting endosomes that ultimately fuse with melanosomes, delivering a cohort of transmembrane melanogenic proteins that include TYR-related protein-1 (TYRP1) and oculocutaneous albinism type 2 (OCA2) (Delevoye et al., 2009; Setty et al., 2008; Setty et al., 2007; Sitaram et al., 2012). BLOC-1 coordinates with the microtubule motor KIF13A and actin polymerization to generate the tubules (Delevoye et al., 2016; Delevoye et al., 2009) and may directly stabilize them (Jani et al., 2021; Lee et al., 2012). Adaptor protein-1 (AP-1) and a cohort of AP-3 sort cargoes and SNARE proteins (including the v-SNARE, VAMP7) into the melanosome-bound tubules (Bowman et al., 2021; Delevoye et al., 2009; Dennis et al., 2015; Theos et al., 2005); AP-1 also binds to and might recruit KIF13A to the tubules (Delevoye et al., 2009; Delevoye et al., 2014; Nakagawa et al., 2000). Despite these advances, we do not yet understand the process of BLOC-1-dependent tubule formation in molecular detail. For example, nothing is known regarding the lipid requirements for engaging BLOC-1 and/or other effectors or for physical stabilization of the tubules.

Among the lipids that might participate in BLOC-1-dependent tubule formation, phosphoinositides are good candidates. Phosphoinositides have essential roles in determining membrane identity, spatio-temporal regulation of membrane trafficking, and membrane remodeling (Balla, 2013; Suetsugu et al., 2014). Their functions in membrane deformation are conferred primarily by their engagement of specific binding proteins that induce or stabilize membrane curvature (Balla, 2013; Suetsugu et al., 2014). In particular, phosphatidylinositol 4-phosphate (PtdIns4P) controls membrane curvature associated with membrane tubules in the endolysosomal system (Levin-

Konigsberg et al., 2019; López-Haber et al., 2020; Ma et al., 2020; McGrath et al., 2021; Rahajeng et al., 2019). PtdIns4P in most cells is primarily present at the plasma membrane, Golgi, and a subset of endosomes (D'Angelo et al., 2008; Tan and Brill, 2014). This distribution is governed by the balanced enzymatic activities of PtdIns4P-generating kinases and phosphoinositide phosphatases. The endosomal PtdIns4P pool is largely produced and maintained by the type II PtdIns-4-kinases, PI4KIIα and PI4KIIβ (Balla and Balla, 2006; Minogue, 2018). Type II PtdIns-4-kinases and PtdIns4P are necessary for the formation of tubules during phagolysosome resolution in macrophages (Levin-Konigsberg et al., 2019), phagosome signaling in dendritic cells (López-Haber et al., 2020), and secretory granule maturation in *Drosophila melanogaster* larval salivary glands (Burgess et al., 2012; Ma et al., 2020). Moreover, both PI4KIIα and PI4KIIβ are required for the proper maturation of Weibel-Palade bodies, LROs of endothelial cells required for hemostasis (Lopes da Silva and Cutler, 2016). These findings strongly suggest a general role for type II PtdIns-4-kinases and PtdIns4P in LRO biogenesis.

How might PtdIns4P and PtdIns-4-kinases integrate with the LRO machinery? Their association with membrane tubules suggests that they might function in BLOC-1-dependent transport pathways. Notably, both PI4KIIα and PI4KIIβ are known binding partners of key pathway components. PI4KIIα binds directly to AP-3 via its dileucine-based sorting motif (Craige et al., 2008; Salazar et al., 2005) and indirectly to BLOC-1 (Salazar et al., 2009), and is targeted to lysosomes and LROs in other cell types in an AP-3-dependent manner (Craige et al., 2008; López-Haber et al., 2020). Similarly, PI4KIIβ binds directly to AP-1 via its dileucine-based sorting signal (Wieffer et al., 2013). Moreover, our companion study shows that BLOC-1 binds to phosphoinositides, including PtdIns4P, on tubular membranes to initiate recycling endosome biogenesis in HeLa cells (Jani et al., 2021). Therefore, we hypothesized that PI4KIIα and/or PI4KIIβ function in BLOC-1-dependent cargo transport to melanosomes by generating PtdIns4P

on the endosomal tubules. Here we tested this hypothesis by using gene silencing and imaging approaches together with biochemical analyses of membrane association. While PI4KIIα and PI4KIIβ likely play redundant roles in BLOC-1-dependent tubule initiation (Jani et al., 2021), our data show that they each play non-redundant roles in generating PtdIns4P on BLOC-1-dependent tubular carriers in melanocytes. These functions are necessary for the stability of the tubules and for cargo delivery to melanosomes. We conclude that type II PtdIns4-kinases play critical general roles in tubule-dependent cargo transport in the biogenesis of multiple LROs.

RESULTS

Type II PtdIns4-kinases are required for melanosomal localization of BLOC-1-dependent cargos.

The biosynthetic delivery of TYRP1 to melanosomes from early endosomal intermediates in melanocytes requires BLOC-1 (Setty et al., 2007). To determine if type II PtdIns-4-kinases function in BLOC-1-dependent cargo transport, we first tested whether depletion of PI4KIIα or PI4KIIβ impacts TYRP1 localization. Immortalized wild-type (WT) melanocytes from C57BL/6J-*Ink4aArf*$^{-/-}$ mice (melan-Ink4a) were transduced with lentiviruses co-expressing a selectable marker (puromycin resistance) and shRNA for PI4KIIα, PI4KIIβ, the core Pallidin subunit of BLOC-1, or a non-target control (NC), and selected for puromycin-resistant cells expressing the shRNAs over 7-14 d. We used two shRNAs with distinct sequences for each target; each chosen shRNA effectively reduced expression of its specific target but did not consistently impact expression of other proteins analyzed (**Fig. S1A-C**). We then assessed TYRP1 steady state localization by confocal immunofluorescence microscopy (IFM) relative to pigment granules visualized by bright field microscopy (**Fig. 1A**-**C**); analyses excluded the crowded perinuclear region of the cell where individual compartments were difficult to distinguish. The majority of TYRP1 in cells treated with control shRNA (shNC, **Fig. 1Aa**-**c, 1B, 1C**), like in untreated cells (Raposo et al., 2001; Setty et al., 2007; Vijayasaradhi et al., 1995), surrounded pigment granules (54.0 ± 10.5% for shNC), apparent by IFM as fluorescent “donuts” filled with black melanin (white arrows) and representing localization to the limiting membrane of mature melanosomes (Raposo et al., 2001). In contrast, TYRP1 localization to peripheral melanosomes was dramatically reduced in cells depleted of PI4KIIα (29.2 ± 14.8% for shPI4KIIα-1, 25.7 ± 14.9% for shPI4KIIα-2, **Fig. 1Ad-f** and **1B**) or PI4KIIβ (26.5 ± 11.9% for shPI4KIIβ-1, 27.1 ± 12.0% for shPI4KIIβ-2; **Fig. 1Ag-i** and **1B**). Instead, TYRP1 localized to punctate structures that did not overlap with pigment granules in these cells (yellow arrowheads). Moreover, many cells depleted of PI4KIIα were significantly hypopigmented, and cells depleted of PI4KIIβ were more modestly hypopigmented (**Fig. 1Ab**, **Ae**, **Ah**), as

confirmed by a quantitative melanin content assay (**Fig. 1F**). Nevertheless, the percentage of remaining melanosomes that were labeled by TYRP1 was reduced in cells depleted of either PI4KIIα or PI4KIIβ relative to control cells (54.8 ± 12.1% for shNC, 28.1 ± 19.2% for shPI4KIIα-1, 23.2 ± 10.5% for shPI4KIIα-2, 31.9 ± 15.5% for shPI4KIIβ-1, 30.2 ± 14.1% for shPI4KIIβ-2, **Fig. 1C**). The reduced pigmentation and TYRP1 localization to melanosomes in PI4KIIα- or PI4KIIβ-depleted cells resembled the phenotype of melanocytes from mice lacking the Pallidin, Muted, or BLOS3 subunit of BLOC-1 (Setty et al., 2007); indeed, TYRP1 overlap with pigment granules was quantitatively similar in cells depleted of Pallidin by shRNA (23.0 ± 14.3% for shPallidin-1, 21.5 ± 13.0% for shPallidin-2, **Figs. 1Aj-l**, **1B**, **S1B, S1C**). These results indicated that both PI4KIIα and PI4KIIβ, like BLOC-1, are required for TYRP1 localization to melanosomes and optimal pigmentation.

Analyses of melanocytes at 30 d post-infection with shRNAs to PI4KIIα or PI4KIIβ showed that, despite consistent target protein depletion, TYRP1 localization to melanosomes was largely restored to baseline levels (**Fig. S1D**, white arrows; **Figs. S1E, S1F**). This likely reflects functional compensation for loss of type II PtdIns-4-kinases over time. Consequently, we chose not to knock out the genes encoding PI4KIIα or PI4KIIβ, and all analyses were performed on cells expressing shRNAs for 7-14 d.

To test whether PI4KIIα or PI4KIIβ depletion impacts other melanosome cargoes, we analyzed the localization of transiently expressed, epitope-tagged forms of OCA2 [a melanosomal chloride channel (Bellono and Oancea, 2014; Sitaram et al., 2009)] and VAMP7 [functions as a v-SNARE in fusion of BLOC-1-dependent transport carriers with melanosomes (Dennis et al., 2016; Tamura et al., 2011)] relative to melanosomes in shPI4KIIα- and shPI4KIIβ-treated cells. Both OCA2 and VAMP7 localize to melanosomes in a BLOC-1-dependent manner (Dennis et al., 2016; Sitaram et al., 2012). Compared with cells expressing control shRNAs in which HA-tagged OCA2 (OCA2-

HA) largely overlapped (49.7 ± 11.0%) with pigment granules (**Fig. 1Da-c** and **1E**, white arrows), OCA2-HA localization was impaired in cells depleted of either PI4KIIα or PI4KIIβ (32.0 ± 10.6% for shPI4KIIα-1 and 29.6 ± 15.5% for shPI4KIIα-2, **Fig. 1Dd-f**; 24.1 ± 16.8% for shPI4KIIβ-1 and 29.5 ± 13.9% for shPI4KIIβ-2, **Fig. 1Dg-i**; **Fig 1E)**. Similar effects of PI4KIIα or PI4KIIβ depletion were observed for GFP-VAMP7 (51.2 ± 10.4% overlap with melanosomes for shNC, white arrows, **Fig. S2Aa-c**; 33.2 ± 12.2% for shPI4KIIα-1 and 32.8 ± 13.9% for shPI4KIIα-2, **Fig. S2Ad-f**; 28.1 ± 14.6% for shPI4KIIβ-1, 31.8 ± 13.5% for shPI4KIIβ-2, **Fig. S2Ag-i; Fig. S2B**). As for TYRP1, the mislocalized OCA2-HA and GFP-VAMP7 were present in punctate structures throughout the cytoplasm (**Figs. 1D, S2A**, yellow arrowheads). Thus, both type II PtdIns-4-kinases in melanocytes are required for effective delivery of OCA2-HA and GFP-VAMP7 to melanosomes and therefore for effective BLOC-1-dependent cargo delivery.

TYRP1 largely mislocalizes to late endosomes and lysosomes in cells depleted of either PI4KIIα or PI4KIIβ.

BLOC-1 is required for TYRP1 and other melanosome cargoes to exit vacuolar endosomes into tubules destined for maturing melanosomes; these cargoes are thus trapped in enlarged early endosomes in BLOC-1-deficient melanocytes (Delevoye et al., 2016; Dennis et al., 2016; Setty et al., 2008; Setty et al., 2007; Sitaram et al., 2012). To determine whether PI4KIIα and PI4KIIβ function at the same step, we defined TYRP1 localization in cells depleted of PI4KIIα or PI4KIIβ. Melanocytes treated with control shRNA or shRNAs to PI4KIIα, PI4KIIβ, or the Pallidin subunit of BLOC-1 were fixed, immunolabeled for TYRP1 and the pan-endosomal t-SNARE syntaxin-13 (STX13), and analyzed by IFM. Whereas STX13 and TYRP1 overlapped minimally in cells treated with control shRNA (20.1 ± 7.6%, **Fig. 2Aa-c**, white arrows, and **Fig. 2B**), they overlapped extensively in the cell periphery in cells depleted of BLOC-1 by Pallidin-specific shRNA (53.8 ± 11.2% for shPallidin-1 and 56.9 ± 9.1% for shPallidin-2, **Fig. 2Aj-l**, yellow arrowheads, and **Fig. 2B**) as previously observed in cells lacking BLOC-1 subunits (Setty et al., 2007). Although the

overlap of TYRP1 with STX13 (yellow arrowheads) in cells depleted of PI4KIIα or PI4KIIβ was higher than in control cells, consistent with some role for the type II PtdIns-4-kinases in initiating BLOC-1-dependent cargo export from endosomes (Jani et al., 2021), the degree of overlap was not as high as in Pallidin knockdown cells (38.3 ± 10.6% for shPI4KIIα-1 and 39.2 ± 12.4% for shPI4KIIα-2, **Fig. 2Ad-f;** 39.8 ± 10.9% for shPI4KIIβ-1 and 39.8 ± 10.2% for shPI4KIIβ-2, **Fig. 2Ag-i; Fig. 2B**). These results indicate that depletion of PI4KIIα or PI4KIIβ partially traps TYRP1 in early endosomes, suggesting that both contribute to BLOC-1-dependent cargo exit from early sorting endosomes but that neither alone is absolutely required.

To determine where the bulk of TYRP1 was mislocalized in cells depleted of PI4KIIα or PI4KIIβ, we tested for TYRP1 overlap with contents of other endolysosomal compartments by IFM. Notably, whereas overlap of peripheral TYRP1 with the late endosomal/ lysosomal membrane protein, LAMP2, is minimal in untreated cells or cell treated with control shRNA (26.5 ± 9.2% **Fig. 2Ca-c**, white arrows, and **Fig. 2D**) – as previously also observed in BLOC-1-deficient ells (Setty et al., 2007) – it was substantially increased (yellow arrowheads) in cells depleted of either PI4KIIα or PI4KIIβ (42.8 ± 11.6% for shPI4KIIα-1 and 46.1 ± 17.0% for shPI4KIIα-2, **Fig. 2Cd-f;** 43.0 ± 12.5% for shPI4KIIβ-1 and 44.5 ± 10.8% for shPI4KIIβ-2, **Fig. 2Cg-i**; **Fig. 2D**). The total fraction of TYRP1 overlapping with pigment granules, early endosomes, and late endosomes/ lysosomes accounted for all of the TYRP1 in the cells, suggesting that little, if any, TYRP1 localizes to other compartments at steady state. These data indicate that in the absence of PI4KIIα or PI4KIIβ, a cohort of TYRP1 is capable of exiting early endosomes but is then mistargeted to late endosomes and lysosomes. Thus, while both type II PtdIns4-kinases play perhaps partially redundant roles in BLOC-1-dependent cargo exit from endosomes, they each have non-redundant functions in an at least partially distinct step from BLOC-1.

PI4KIIα and PI4KIIβ functions in TYRP1 trafficking require their lipid kinase activity and binding to adaptor proteins.

To ensure that TYRP1 mislocalization was not an off-target effect of expressing the shRNAs to PI4KIIα and PI4KIIβ, we assessed whether TYRP1 localization to melanosomes was restored by overexpressing shRNA-resistant PI4KIIα or PI4KIIβ. We transduced WT mouse melan-Ink4a melanocytes with retroviruses encoding GFP-tagged human WT PI4KIIα or PI4KIIβ, selected for stable transduction for at least two weeks, and then transduced these cells with lentiviruses expressing shRNA specific to mouse PI4KIIα or PI4KIIβ to deplete the endogenous target protein. One week later, the cells were analyzed by IFM and bright field microscopy to define TYRP1 localization relative to pigment granules. Unlike melanocytes expressing shRNA to PI4KIIα or PI4KIIβ alone (**Fig. 3B**, **Fig. 4B**) in which the degree of TYRP1 overlap with pigment granules was minimal (yellow arrowheads), co-expression of PI4KIIα-WT-GFP with shPI4KIIα-1 (**Fig. 3C**) or of PI4KIIβ-WT-GFP with shPI4KIIβ-2 (**Fig. 4C**) resulted in a significant fraction of cells with a WT pattern of TYRP1 localizing largely in donut-like structures around pigment granules (compare white arrows in **Fig. 3A** with **3C** and **Fig. 4A** with **4C**; **Fig. 3G** and **4G**, 50.4 ± 12.6% for shNC, 38.4 ± 12.9% for shPI4KIIα-1+ PI4KIIα-WT-GFP, 36.5 ± 12.5% for shPI4KIIβ-2+ PI4KIIβ-WT-GFP). Immunoblotting showed that the transgenes were expressed efficiently and that shRNA to endogenous mouse PI4KIIα (**Fig. 3H**) and PI4KIIβ (**Fig. 4H**) efficiently reduced target protein expression even in the presence of excess human GFP-tagged transgene. These data indicate that expression of shRNA-resistant GFP-tagged target protein at least partially restored TYRP1 localization in cells treated with shRNAs to endogenous PI4KIIα or PI4KIIβ, and thus that the impaired TYRP1 localization in shRNA-treated cells was a direct result of target protein depletion. The failure of GFP-tagged PI4KIIα-WT and PI4KIIβ-WT to fully restore TYRP1 localization might reflect either partial interference with kinase activity by the C-terminal GFP fusion protein or an artifact of kinase overexpression. Surprisingly, overexpression of either PI4KIIβ-WT-GFP in PI4KIIα knockdown cells or of PI4KIIα-WT-GFP in PI4KIIβ knockdown cells restored TYRP1

localization to the same degree as re-expression of the knocked-down kinase (white arrows; 35.3 ± 16.2% for shPI4KIIα-1+ PI4KIIβ-WT-GFP, **Fig. 3Fu-x**; 34.7 ± 15.7% for shPI4KIIβ-2+ PI4KIIα-WT-GFP, **Fig. 4Fu-x**; **Figs. 3G, 4G**, **4I**). While this result superficially contradicts the requirement for both endogenous PI4KIIα and PI4KIIβ in TYRP1 trafficking, it might reflect cross-compensation by the overexpression of PtdIns-4-kinase activity in adjacent endosomal domains.

The ability of GFP-tagged PI4KIIα-WT or PI4KIIβ-WT to rescue TYRP1 localization in shRNA-treated cells allowed us to determine if PI4KIIα and PI4KIIβ functions in melanosome cargo transport require their kinase activities and binding to their respective adaptor proteins. We generated kinase-dead mutants [PI4KIIα-D308A and PI4KIIβ-D304A; (Balla et al., 2002)] and AP binding-deficient mutants [AP-3-binding-deficient PI4KIIα-L61, 62A and AP-1-binding-deficient PI4KIIβ-L29, 30A; (Craige et al., 2008; Wieffer et al., 2013)], expressed them stably in WT mouse melanocytes, and then knocked down the endogenous corresponding mouse kinase for 7 d prior to analysis of TYRP1 localization by IFM. Despite effective expression of all mutants as assessed by both IFM (**Fig. 3D**, **E**; **Fig. 4D**, **E**) and immunoblotting (**Fig. 3H; Fig. 4H**), neither the kinase dead nor AP binding mutants of either PI4KIIα or PI4KIIβ restored TYRP1 localization to pigment granules in cells depleted of the endogenous mouse target; the degree to which TYRP1 overlapped with pigment granules in shRNA-treated cells was essentially the same whether or not the kinase-dead or AP-binding mutants were co-expressed (yellow arrowheads; 26.2 ± 15.0% for shPI4KIIα-1; 22.1 ± 17.3% for shPI4KIIα-1+ PI4KIIα-D308A-GFP; 23.9 ± 15.8% for shPI4KIIα-1+ PI4KIIα-L61, 62A-GFP; 24.4 ± 12.9% for shPI4KIIβ-2; 19.9 ± 13.7% for shPI4KIIβ-2+ PI4KIIα-D304A-GFP; 21.6 ± 16.9% for shPI4KIIβ-2+ PI4KIIα-L29, 30A-GFP; **Figs. 3G, 4G**). Interestingly, whereas GFP-tagged PI4KIIα-WT (**Fig. 3Ci**) and kinase dead PI4KIIα-D308A (**Fig. 3Dm**) were both localized predominantly to punctate cytoplasmic structures that likely represent endosomes (see below), and GFP-tagged PI4KIIβ-WT (**Fig. 4Ci**) and kinase dead PI4KIIβ-D304A (**Fig. 4Dm**) were both localized predominantly to the perinuclear region and a few cytoplasmic punctae, the

AP-3-binding mutant PI4KIIα-L61, 62A (**Fig. 3Eq**) and the AP-1-binding mutant PI4KIIβ-L29, 30A (**Fig. 4Eq**) largely localized to the plasma membrane with minimal intracellular labeling. These data suggest that both PI4KIIα and PI4KIIβ require both their kinase activity and their interaction with APs to promote TYRP1 localization, and that recruitment of PI4KIIα and PI4KIIβ to endolysosomal membranes requires binding to AP-3 (PI4KIIα) or AP-1 (PI4KIIβ).

Non-redundant requirement for PI4KIIα and PI4KIIβ in tubular transport to melanosomes is downstream of BLOC-1.

Because depletion of either PI4KIIα or PI4KIIβ did not trap TYRP1 within early endosomes to the same degree as depletion or knockout of BLOC-1 subunits, we hypothesized that BLOC-1 and type II PtdIns4-kinases have sequential non-redundant functions in melanosome cargo transport. In this scenario, BLOC-1 would facilitate cargo exit from vacuolar early sorting endosomes into nascent tubular carriers and type II PtdIns4-kinases would independently promote ensuing steps in tubule stabilization and/or targeting towards melanosomes. If this were true, then knockdown of PI4KIIα or PI4KIIβ in BLOC-1-deficient cells should yield a BLOC-1-deficiency cargo localization phenotype in which TYRP1 is trapped in early endosomes. BLOC-1 knockout (BLOC-1$^{-/-}$) melanocytes derived from Pallid mice, which lack the Pallidin (*Bloc1s6*) subunit and thus fail to assemble BLOC-1, were treated with shNC, shPI4KIIα or shPI4KIIβ. They were then analyzed by triple labeling IFM using antibodies to TYRP1, either PI4KIIα or PI4KIIβ (data not shown) to validate protein depletion, and transferrin receptor (TfR) to identify early sorting and recycling endosomes [note that TfR at steady state overlaps with STX13 but not TYRP1 in WT melanocytes, and with both STX13 and TYRP1 in BLOC-1$^{-/-}$ melanocytes (**Fig S3**), and is used instead of STX13 in this experiment to allow for triple labeling]. Consistent with previously published data (Delevoye et al., 2016; Setty et al., 2008; Setty et al., 2007) and **Fig. 2A**, TYRP1 overlapped substantially with TfR in control BLOC-1$^{-/-}$ cells treated with shNC (yellow arrowheads; 49.9 ± 7.5%, arrowheads in **Fig. 5Aa-c** and **5B).** Knock down of PI4KIIα or PI4KIIβ in these cells with

either of two shRNAs each did not significantly alter the degree of TYRP1/ TfR overlap (yellow arrowheads; 50.0 ± 8.0% for shPI4KIIα-1 and 51.9 ± 10.7% for shPI4KIIα-2, **Fig. 5Ad-f;** 52.0 ± 8.8% for shPI4KIIβ-1 and 51.3 ± 10.5% for shPI4KIIβ-2, **Fig. 5Ag-i**; **Fig. 5B**). These results indicate that TYRP1 is trapped in early endosomes in BLOC-1-deficient cells regardless of the expression of PI4KIIα or PI4KIIβ, and support the conclusion that PI4KIIα and PI4KIIβ have unique functions downstream of BLOC-1 in cargo transport to melanosomes.

One potential function for PI4KIIα and PI4KIIβ is to provide a pool of PtdIns4P sufficient to recruit or stabilize BLOC-1 and other effectors of tubular transport on membranes. Indeed, our companion paper (Jani et al., 2021) shows that PtdIns4P is sufficient to stabilize recombinant BLOC-1 association with tubular membranes *in vitro*. To test whether the recruitment of BLOC-1 and other effectors requires either type II PtdIns-4-kinase independently, we performed subcellular fractionation of WT melanocytes treated with shNC or shRNAs to PI4KIIα or PI4KIIβ, and assessed the relative association of BLOC-1, AP-1, and AP-3 with membrane and cytosolic fractions by immunoblotting for the Pallidin, AP-1γ , and AP-3μ subunits, respectively (**Fig. 5C**, **D**). Depletion of either PI4KIIα or PI4KIIβ neither substantially nor significantly reduced BLOC-1 membrane association (58.2 ± 12.3% for shNC, 53.6 ± 13.9% for shPI4KIIα-1 and 45.1 ± 13.9% for shPI4KIIα-2, 60.8 ± 23.2% for shPI4KIIβ-1 and 58.7 ± 11.9% for shPI4KIIβ-2, **Fig. 5C, D**); the decrease caused by shPI4KIIα-2 might reflect an off-target effect since this shRNA was not as efficient as shPI4KIIα-1 in reducing PI4KIIα levels (**Fig. S1A and S1C**) and also slowed cell growth**.** Similarly, knockdown of either PI4KIIα or PI4KIIβ had essentially no effect on the membrane association of AP-1 (75.3 ± 5.2% for shNC, 70.4 ± 7.0% for shPI4KIIα-1 and 61.5 ± 5.7% for shPI4KIIα-2, 72.6 ± 8.8% for shPI4KIIβ-1 and 74.8 ± 6.1% for shPI4KIIβ-2, **Fig. 5C**, **D**) or AP-3 (72.3 ± 6.7% for shNC, 70.0 ± 7.5% for shPI4KIIα-1 and 64.9 ± 4.3% for shPI4KIIα-2, 71.3 ± 5.5% for shPI4KIIβ-1 and 71.0 ± 5.2% for shPI4KIIβ-2, **Fig. 5C**, **D**). We therefore conclude that neither type II PtdIns4-kinases is uniquely required for the association of BLOC-1, AP-3 or

AP-1 with membranes, and that each has an independent function downstream of BLOC-1 in tubular transport from early endosomes to melanosomes.

PI4KIIα and PI4KIIβ function sequentially to enrich PtdIns4P on tubular endosomal domains

If PI4KIIα and PI4KIIβ directly regulate BLOC-1-dependent cargo transport and function non-redundantly downstream of BLOC-1, then they and their product, PtdIns4P, should be present on the tubular carriers through which cargo is transferred from endosomes to melanosomes. To test this, we utilized live-cell microscopy to observe the dynamics of GFP-tagged PI4KIIα, PI4KIIβ or a PtdIns4P probe relative to the formation and extension of tubules labeled by mCherry-tagged STX13, which labels the entire early endosomal network including the tubular carriers (Bowman et al., 2021; Delevoye et al., 2016; Dennis et al., 2015). To detect PtdIns4P, we exploited a GFP-tagged form of P4C-SidC, a PtdIns4P-binding domain derived from the secreted SidC effector protein of *Legionella pneumophila* (Dolinsky et al., 2014; Weber et al., 2018; Weber et al., 2014) (hereafter referred to as P4C). GFP-tagged proteins were transiently expressed in WT melanocytes stably expressing mCherry-STX13, and cells were analyzed the next day. Dual-view live-cell spinning disc microscopy (Kinosita et al., 1991) allowed us to simultaneously detect mCherry- and GFP-tagged components in real time, and thus to determine their order of appearance during the process of tubule formation from STX13-labeled endosomal vacuoles. Still images from image streams show that GFP-tagged PI4KIIα, PI4KIIβ, and P4C each labeled punctate structures and tubules that were largely localized to mCherry-STX13-positive structures (yellow arrowheads in insets, **Fig. 6A**-**C**), consistent with previous studies (Balla et al., 2002; Craige et al., 2008; Dong et al., 2016; Jovic et al., 2014; Ma et al., 2020; Wieffer et al., 2013). Since the majority of STX13-labeled tubules in melanocytes are BLOC-1-dependent (Delevoye et al., 2016), the tubules that were decorated with both mCherry-STX13 and either PI4KIIα-GFP or PI4KIIβ-GFP likely corresponded to the BLOC-1-dependent tubular carriers. Additional tubules

were labeled only by PI4KIIα-GFP, PI4KIIβ-GFP, or GFP-P4C-SidC (data not shown), suggesting that type II PtdIns4-kinases associate with membrane tubules outside the early endosomal system in melanocytes. In addition, as expected, P4C also labeled the plasma membrane and the Golgi area (**Fig. 6C**; see also **Fig. 8Aa-c**). The data suggest that PI4KIIα, PI4KIIβ, and their product PtdIns4P are present on the early endosomal tubular structures that ferry cargo to melanosomes.

If both PI4KIIα and PI4KIIβ are present on membrane tubules, why are they both necessary for cargo delivery to melanosomes? We reasoned that they might associate with the tubules in a temporally distinct manner. We therefore analyzed the dual-view image streams of cells expressing mCherry-STX13 and PI4KIIα-GFP or PI4KIIβ-GFP, focusing on the temporal association of each PI4KII isoform relative to the onset of tubule formation from round STX13-containing early endosomes. In in 22 out of 24 instances in which the source endosome and a nascent tubule were visualized, PI4KIIα-GFP was present on the body of mCherry-STX13-containing endosomes prior to the onset of tubule formation (**Fig. 7A**, white arrowheads), and labeling for PI4KIIα-GFP within the nascent tubule coincided with labeling for mCherry-STX13 from the appearance of a small protrusion (**Fig. 7A**, yellow arrowhead, 0s) to the extension of a long tubule (**Fig. 7A,** yellow arrowheads, 0.4-4s). This indicated that PI4KIIα is sorted into the tubular carriers during their formation. By contrast, the kinetics of PI4KIIβ-GFP association with tubules was distinct. In 20 out of 26 instances, PI4KIIβ-GFP was not detectable on the mCherry-STX13-labeled nascent tubules (**Fig. 7B**; tubule initiates at white arrowhead), but rather appeared as the tubule extended and accumulated along the length of the tubules (**Fig. 7B**, 1.6-2.4s between white and yellow arrowheads). In those cases where PI4KIIβ-GFP was detected on the source endosome prior to tubulation, it was typically present in a subdomain (**Fig. 7B**, white arrowheads) and was more enriched on the tubules. These results indicate that PI4KIIβ, unlike

PI4KIIα, associates with established tubules, and suggest that PI4KIIβ functions at a later step of tubule dynamics than PI4KIIα.

Consistent with the combined distribution of PI4KIIα-GFP and PI4KIIβ-GFP on the tubules, dual-view analysis showed that their product, PtdIns4P (visualized with GFP-P4C-SidC), was present throughout the lifetime of the mCherry-STX13-positve tubules from the onset of tubule formation through tubule extension (**Fig. 7C**, all panels from white arrows to yellow arrowheads). This correlates the presence of PtdIns4P with tubule elongation and stabilization. Tubules labeled by P4C but not mCherry-STX13 were also observed moving towards the plasma membrane and likely represent Golgi-derived carriers (Graham and Burd, 2011; Highland and Fromme, 2021; Stalder and Gershlick, 2020).

PI4KIIα and PI4KIIβ are both required for maintenance of the endosomal PtdIns4P pool.

To test whether PI4KIIα and PI4KIIβ activity was responsible for PtdIns4P on vacuolar endosomes and endosomal tubules, we assessed the distribution of PtdIns4P in PI4KIIα- or PI4KIIβ-depleted cells using both P4C and a second more widely used probe, GFP-P4M-SidMx2 (hereinafter referred to as P4Mx2), which contains a tandem repeat of the PtdIns4P binding domain of the secreted SidM protein from *Legionella pneumophila* (Hammond et al., 2014). Because expression of both probes by transient transfection was heterogenous, we expressed each probe stably in WT melanocytes and then treated the cells with control, PI4KIIα- or PI4KIIβ-directed shRNAs. Cells were then analyzed by spinning disk confocal microscopy.

P4Mx2 primarily detected a diffuse pool of PtdIns4 that likely represents the plasma membrane (note the intense labeling of filopodia and lamellipodia), with additional sparse labeling in the Golgi region and moderate punctate labeling of perinuclear and cytoplasmic structures (**Fig. S4Aa**). Knockdown of either PI4KIIα or PI4KIIβ particularly diminished punctate labeling (**Fig. S4Ab, c**),

as indicated by the reduced standard deviation (SD) of fluorescent intensity throughout the cell (18.0 ± 11.0 for shNC, 9.5 ± 2.3 for shPI4KIIα-1, 10.2 ± 3.9 for shPI4KIIβ-1, **Fig. S4B**). PI4KIIβ knockdown additionally tended to diminish the diffuse plasma membrane labeling; because the SD values are affected by the overall signal intensity, we normalized SD to the cytoplasmic mean intensity, generating a coefficient of variation (44.6 ± 11.6% for shNC, 32.6 ± 5.6% for shPI4KIIα-1, 45.9 ± 10.5% for shPI4KIIβ-1, **Fig. S4C**). This analysis showed that P4Mx2 intensity was less variable in PI4KIIα-depleted cells than in control or PI4KIIβ-depleted cells. We thus conclude that PI4KIIα is specifically responsible for the majority of the punctate (likely endolysosomal) PtdIns4P pool, but that PI4KIIβ contributes to both the punctate and plasma membrane pools of PtdIns4P.

Because P4C extensively labeled endosomal PtdIns4P and detected PtdIns4P on tubules (**Figs. 6**, **7**), we exploited this probe to define the impact of PI4KIIα and PI4KIIβ depletion on the tubular pool of PtdIns4P. To define endosomal tubules, cells stably expressing P4C and either control, PI4KIIα-, or PI4KIIβ-specific shRNAs were transiently transfected to express mCherry-STX13 prior to dual-view live-cell spinning disc microscopy analysis. As also seen in transient transfections (**Fig. 6**), stably expressed P4C in shNC cells generally localized to the plasma membrane, Golgi, and perinuclear and peripheral endosomal compartments (**Fig. 8Aa**). Depletion of PI4KIIα or PI4KIIβ resulted in an apparent diminution of P4C-labeled puncta in the periphery and an accumulation in the perinuclear region (**Fig. 8Ad, g**); unlike in cells that did not express P4C (**Fig. 2A**), this was accompanied by a perinuclear accumulation of STX13-labeled endosomes (**Fig. 8Ae, h**), perhaps due to exacerbation of altered endosomal dynamics by shielding of remaining PtdIns4P. Concomitantly, fewer tubular structures that were labeled by P4C (15.9 ± 4.0 for shNC, **Fig. 8Aa**; 10.6 ± 2.9 for shPI4KIIα-1, **Fig. 8Ad**; 10.3 ± 4.8 for shPI4KIIβ-1, **Fig. 8Ag**; **Fig. 8B**) or doubly labeled by both P4C and mCherry-STX13 (10.5 ± 2.8 for shNC, **Fig. 8Ac**; 6.5 ± 1.8 for shPI4KIIα-1, **Fig. 8Af**; 5.3 ± 3.0 for shPI4KIIβ-1, **Fig. 8Ai**; **Fig. 8C**) were observed in PI4KIIα- and PI4KIIβ-depleted cells (white arrowheads) than in control cells (yellow

arrowheads). The percentage of tubules that were doubly labeled by both P4C and mCherry-STX13 relative to total P4C tubules did not significantly change in PI4KIIα- and PI4KIIβ-depleted cells (66.6 ± 11.9% for shNC, 58.5 ± 15.0% for shPI4KIIα-1, 54.8 ± 19.8% for shPI4KIIβ-1, **Fig. 8D**), although they trended lower, particularly when cells were binned into high (60-100%), moderate (40-60%), and low (0-40%) levels of overlap (**Fig. 8E**). These data suggest that both PI4KIIα and PI4KIIβ contribute to the generation of PtdIns4P on membrane tubules emanating from both early endosomes and also from other compartments, such as lysosomes (Levin-Konigsberg et al., 2019).

PI4KIIα and PI4KIIβ are needed to support the formation of effective tubular carriers.

What role might local PtdIns4P production by PI4KIIα and PI4KIIβ on membrane tubules serve? Given that PI4KIIα and PI4KIIβ localization correlated with tubule formation and elongation respectively, we tested whether PI4KIIα and PI4KIIβ are required for proper tubule dynamics in melanocytes. WT melanocytes that stably expressed mCherry-STX13 were treated with control, PI4KIIα-, or PI4KIIβ-specific shRNAs, and the effects on STX13-positive tubular structures were assessed by live-cell spinning disk confocal microscopy. In shNC-treated cells, as observed in untreated cells [**Figs. 6** and **7** and (Bowman et al., 2021; Dennis et al., 2016; Dennis et al., 2015)], numerous long and dynamic STX13-positive tubules were detected throughout the cytoplasm (fluorescent images shown in **Fig 9Aa and Ab**; skeletonized images shown in **Fig. 9Ac and Ad**). Although cells depleted of PI4KIIα or PI4KIIβ also harbored dynamic tubules, relative to shNC cells they were fewer in number (24.4 ± 5.3 for shNC, **Fig. 9Aa-d**; 16.9 ± 4.0 for shPI4KIIα-1, **Fig. 9Ba-d**; 20.1 ± 5.7 for shPI4KIIβ-2, **Fig. 9Ca-d**; **Fig. 9D**) and less enriched in the number and percentage of tubules longer than 1 μm (3.7 ± 0.8, 15.7 ± 3.5% for shNC; 1.7 ± 0.8, 9.8 ± 3.7% for shPI4KIIα-1; 2.4 ± 0.8, 12.1 ± 3.3% for shPI4KIIβ-2; **Fig. 9E**, **9F**), which typically contact melanosomes (Bowman et al., 2021; Dennis et al., 2015). The average length of the tubules was also reduced in cells depleted of PI4KIIα or PI4KIIβ (663.1 ± 60.0 nm for shNC, 573.9 ± 43.1 nm

for shPI4KIIα-1, 609.0 ± 41.7 nm for shPI4KIIβ-2, **Fig. 9G**). This suggests that tubules effective in contacting melanosomes are specifically impaired by PI4KIIα or PI4KIIβ deficiency. The reduction in tubule number and length was more severe in cells depleted of PI4KIIα than in cells depleted PI4KIIβ (**Fig. 9E**), consistent with the association of PI4KIIα with nascent tubules and the later association of PI4KIIβ, but seemed to be less severe than has been previously observed in BLOC-1$^{-/-}$ cells (Bowman et al., 2021; Delevoye et al., 2016). These results indicate that PI4KIIα and PI4KIIβ are required sequentially in tubule elongation and/or stabilization, subsequent to BLOC-1-dependent tubule formation.

DISCUSSION

BLOC-1-dependent endosomal tubular carriers play an essential role in cargo delivery to maturing melanosomes, but how lipid composition regulates tubule formation and dynamics was not known. Here, we show that the type II PtdIns-4-kinases, PI4KIIα and PI4KIIβ, are recruited to the tubular endosomal carriers where they cooperate to generate local pools of PtdIns4P. While PI4KIIα and PI4KIIβ likely play redundant roles in PtdIns4P generation for BLOC-1 concentration and tubule initiation (Jani et al., 2021), the tubular PtdIns4P pools are required after tubule formation for tubule stability and for ultimate cargo delivery to melanosomes. Both the kinase activity and adaptor binding properties of PI4KIIα and PI4KIIβ are necessary for these functions. Reduced expression of either PI4KIIα or PI4KIIβ impairs tubular carrier dynamics, resulting in the mistargeting of melanosomal cargos primarily to late endosomes and lysosomes and consequent impaired melanin production. Our results thus support a model in which PI4KIIα on newly generated endosomal tubules and PI4KIIβ on the growing tubules, recruited by AP-3 and AP-1 respectively, generate local PtdIns4P to ensure effective tubular cargo transport to melanosomes (**Fig. 9H**). This model may have broader implications for tubule-dependent cargo transport within the endomembrane system and for LRO biogenesis in general.

In melanocytes, BLOC-1 and the kinesin-3 microtubule motor heavy chain KIF13A are required to generate membrane tubules of long length and lifetime that facilitate transport of selected cargoes to melanosomes (Delevoye et al., 2016; Dennis et al., 2016; Dennis et al., 2015). BLOC-1 in other systems cooperates with PI4KIIα in endosomal trafficking (Gokhale et al., 2012; Larimore et al., 2011; Salazar et al., 2009), but how tubule formation is mechanistically linked to type II PtdIns-4-kinase activity was not understood. Our live-cell imaging results show that PtdIns4P is present over the entire length and lifetime of the BLOC-1-dependent tubules. While both PI4KIIα and PI4KIIβ are detected on the early endosomal vacuoles from which the tubules

emerge, they are also present within distinct domains of the tubules themselves. Accordingly, depletion of either PI4KIIα or PI4KIIβ by shRNAs impaired both the number and length of tubules at steady state. Thus, continuous PtdIns4P generation by PI4KIIα and PI4KIIβ coincides with and is necessary for tubule initiation, extension, and stabilization. The less dramatic effect of PI4KIIα or PI4KIIβ depletion on tubule number than BLOC-1 depletion (Delevoye et al., 2016) likely reflects redundancy in this step by the two type II PtdIns-4-kinases (Jani et al., 2021). The association of PtdIns4P with tubule formation in melanocytes is consistent with previous observations of PtdIns4P on tubules associated with endosomal recycling in HeLa cells (Jovic et al., 2009) and in trafficking from a variety of LROs in different cell types (Domingues et al., 2016; Levin-Konigsberg et al., 2019; López-Haber et al., 2020; Ma et al., 2020). How PtdIns4P might facilitate tubule stability or extension is not entirely clear, but most likely PtdIns4P serves as a platform to recruit membrane bending proteins (Kitamata et al., 2020). These may include BLOC-1 itself [(Jani et al., 2021); see below] and/or other PtdIns4P-binding proteins such as EHD1 or DRG2 (Jovic et al., 2009; Ma et al., 2020; Mani et al., 2017). Alternatively, PtdIns4P might be required to concentrate KIF13A either indirectly via clustering its adaptor AP-1 (Wang et al., 2003) or directly, consistent with the role of PtdIns(4,5)P_2 in clustering KIF1A and KIF5B to drive membrane transport and tubulation (Du et al., 2016; Klopfenstein et al., 2002).

The most surprising finding to us is the observation that two PtdIns-4-kinases of the same family, PI4KIIα and PI4KIIβ, are both required in a non-redundant fashion for extension and/or stability of the same tubular transport carriers. We show that depletion of either PI4KIIα or PI4KIIβ reduces the endosomal pool of PtdIns4P, particularly on the tubules. As a consequence, the number and size of STX13-positive tubules are reduced and melanosome cargo transport is impaired. As in other cell types (Balla et al., 2002; Craige et al., 2008; Jovic et al., 2014; Ma et al., 2020; Wieffer et al., 2013), both PI4KIIα and PI4KIIβ in melanocytes localized largely to early endosomes and

derived tubules, but their subdomain distribution was strikingly distinct; PI4KIIα associated with tubules during their formation (and thus might play the predominant role in tubule initiation), whereas PI4KIIβ mainly accumulated on the tubules after tubule formation and extension. Correlating with this distinction, tubules were shorter upon depletion of PI4KIIα than upon depletion of PI4KIIβ. Together, these data suggest that PI4KIIα and PI4KIIβ each act specifically and non-redundantly to ensure that PtdIns4P levels are maintained throughout tubule elongation. Because PI4KIIα function and localization required its determinant for binding to AP-3, we speculate that PI4KIIα is recruited by AP-3 on budding regions of vacuolar endosomes, where a BLOC-1-AP-3 super-complex (Di Pietro et al., 2006; Salazar et al., 2006; Salazar et al., 2009) facilitates tubule initiation and SNARE and cargo sorting into the nascent tubules (Bowman et al., 2021). Similarly, PI4KIIβ function and localization required its determinant for binding AP-1; we thus further speculate that PI4KIIβ is recruited to the growing tubule by AP-1 bound to KIF13A as KIF13A extends the tubule along microtubules (Campagne et al., 2018; Delevoye et al., 2016; Delevoye et al., 2009; Delevoye et al., 2014). Although we did not observe any significant defects in membrane association of BLOC-1, AP-3, or AP-1 in PI4KIIα- or PI4KIIβ-depleted cells, given that both BLOC-1 (Jani et al., 2021) and AP-1 (Wang et al., 2003) bind PtdIns4P, it is likely that the pool of PtdIns4P generated by PI4KIIα or PI4KIIβ feeds back to concentrate BLOC-1 and AP-1, respectively, on the tubules. Although we found that overexpression of GFP-tagged PI4KIIα in cells depleted of PI4KIIβ or of GFP-tagged PI4KIIβ in cells depleted of PI4KIIα restored cargo localization to melanosomes, we reason that excess local PtdIns4P produced by the overexpressed PI4KII paralogue can diffuse to sites where the absent PI4KII paralogue would normally produce a more limited pool.

PI4KIIα and PI4KIIβ together are needed in a likely redundant manner to initiate BLOC-1-dependent tubule formation (Jani et al., 2021). This is likely mediated by a cohort of both PI4KIIα

and PI4KIIβ that localize to endosomal vacuoles and thus might generate PtdIns4P on the vacuoles during the initiation of tubule formation by concentrating and/or recruiting BLOC-1, as has been shown in HeLa cells by Jani et al (Jani et al., 2021). Our data extend the roles of the type II PtdIns-4-kinases and suggest that the non-redundant requirement for both PI4KIIα and PI4KIIβ in tubule formation and cargo transport to melanosomes temporally follow the requirement for BLOC-1. This conclusion is supported by: (a) the exit of BLOC-1-dependent melanosome cargoes from early endosomes in cells depleted of PI4KIIα or PI4KIIβ but not in cells depleted of BLOC-1; (b) the entrapment of cargo in early endosomes in cells lacking both BLOC-1 and either PI4KIIα or PI4KIIβ; (c) the lack of a significant reduction in BLOC-1 recruitment to membranes in cells depleted of PI4KIIα or PI4KIIβ; and (d) the more modest impairment in tubule number and length in cells depleted of PI4KIIα or PI4KIIβ relative to BLOC-1-deficient cells (Bowman et al., 2021; Delevoye et al., 2016). This is consistent with the notion that BLOC-1 participates in the recruitment of PI4KIIα, perhaps as part of a BLOC-1-AP-3 super-complex (Di Pietro et al 2006; Salazar et al 2006). Our data thus reveal an additional requirement for PtdIns4P in the maintenance and extension of the tubules at a stage following BLOC-1-dependent tubule initiation, also consistent with the live-cell imaging data in Jani et al (Jani et al., 2021). Our efforts to deplete both enzymes in melanocytes by shRNAs were unsuccessful, but future studies using knockout/ knockdown approaches might be used to validate an early requirement for endosomal PtdIns4P in BLOC-1 recruitment in melanocytes.

Our data show that both type II PtdIns-4-kinases are necessary for the ultimate delivery of BLOC-1-dependent cargoes to melanosomes. Depletion of either PI4KIIα or PI4KIIβ resulted in ultimate localization to late endosomes and lysosomes for at least one cargo. This result is not likely a reflection of improper sorting of cargo or SNARE proteins into the nascent tubules, as these are mediated by the interaction of sorting signals with AP-1, AP-3, and/or BLOC-1 (Bowman et al.,

2021; Delevoye et al., 2009; Sitaram et al., 2012; Theos et al., 2005), which were still recruited to membranes in PI4KIIα- or PI4KIIβ-depleted cells. Moreover, depletion of PI4KIIα or PI4KIIβ in BLOC-1-deficient cells led to complete retention within the early endosomal system, indicating that missorting to late endosomes/ lysosomes required BLOC-1 activity and thus likely also tubule initiation. Rather, we interpret the mistargeting of cargo in PI4KIIα or PI4KIIβ-depleted cells to indicate that the short tubules in these cells are insufficient to support effective cargo delivery to melanosomes. This would suggest that the tubules not only serve as a cargo exit point from early endosomal vacuoles, but that their lengths and lifetimes are critical for the ultimate fusion of cargo-carrying membranes with maturing melanosomes and ensuing cargo delivery (Delevoye et al., 2009). This might reflect (a) the long distance needed for cargo to travel from endosomes to peripheral melanosomes or (b) a requirement for selective microtubule-driven processes to ensure that the cargo carriers encounter melanosomes for fusion prior to late endosomes or lysosomes. Intriguingly, the defect in TYRP1 delivery to melanosomes in PI4KIIα- or PI4KIIβ-depleted cells was more severe than that of OCA2 and VAMP7, even though all three cargoes are BLOC-1-dependent (Dennis et al., 2016; Setty et al., 2007; Sitaram et al., 2012). This might reflect a difference in the adaptor requirements for cargo sorting; while TYRP1 relies on AP-1 for sorting to melanosomes, OCA2 and VAMP7 rely on AP-3, which also mediates a distinct BLOC-1-independent cargo transport pathway to melanosomes (Theos et al., 2005). Testing this possibility will require additional analyses of cargo sorting upon PI4KIIα- or PI4KIIβ-depletion in AP-3-deficient melanocytes.

PtdIns4P plays a critical role in membrane dynamics and trafficking to control cargo transport, membrane identity, and organelle contacts generally within the endomembrane system (D'Angelo et al., 2008; Tan and Brill, 2014). Our study extends several others in documenting a specific adaptation of PtdIns4P dynamics within the endomembrane system of specialized cell types for

the maturation of LROs. In dendritic cells and macrophages, PI4KIIα is required to generate PtdIns4P and to form tubules from phagolysosomes, a type of LRO (Bowman et al., 2019), to promote antigen presentation or phagosome resolution (Levin-Konigsberg et al., 2019; López-Haber et al., 2020; Mantegazza et al., 2014). In endothelial cells, both PI4KIIα and PI4KIIβ are necessary for the proper proteolytic maturation and assembly of von Willebrand factor in Weibel-Palade bodies (Lopes da Silva and Cutler, 2016). In *Drosophila melanogaster* salivary glands, the PI4KII orthologue is required to promote PtdIns4P accumulation on secretory granules and the formation of retrograde tubules needed for secretory granule maturation (Ma et al., 2020). Our results extend these studies by documenting a requirement in melanocytes for both mammalian type II PtdIns-4-kinases at distinct stages of membrane tubule-dependent anterograde cargo transport from endosomes to maturing melanosomes. Together, these studies suggest that the formation of PtdIns4P-enriched tubules is a general feature in the maturation of LROs.

MATERIALS AND METHODS

Reagents

Unless otherwise indicated, chemicals were obtained from Sigma-Aldrich or Fisher Bioreagents. Tissue culture reagents and blasticidin were from Life Technologies/Thermo Fisher Scientific. Puromycin was from Takara Bio. Hygromycin B and protease inhibitors were from Roche. Odyssey Blocking Buffer was from LI-COR. Gene amplification primers were from Integrated DNA Technologies. Phusion polymerase, restriction enzymes, T4 DNA ligase and the Gibson Assembly Cloning Kit were from New England Biolabs.

Antibodies

Primary monoclonal antibodies used and their sources (indicated in parentheses) were: mouse anti-TYRP1 (TA99/Mel-5, American Type Culture Collection; Rockville, MD); mouse anti-γ-Tubulin (GTU-88, Sigma); mouse anti-γ-adaptin (BD 610385); rabbit anti-AP3M1 (ab201227; Abcam); rat anti–mouse LAMP2 (GL2A7, Abcam); rat anti-mouse TfR (CD71, BD 553264); and rat anti-HA (3F10, Roche 11867423001). Primary polyclonal antibodies used and their sources were: rabbit anti-STX13 (a kind gift of Rytis Prekeris, Univ. of Colorado, Denver, CO, USA)(Prekeris et al., 1998); rabbit anti-pallidin (a kind gift of Juan Bonifacino, National Institute of Child Health and Human Development, Bethesda, MD, USA)(Moriyama and Bonifacino, 2002); rabbit anti-PI4KIIα and anti-PI4KIIβ (kind gifts of Pietro De Camilli, Yale Univ., New Haven, CT, USA) (Guo et al., 2003); and rabbit anti-GFP (PABG1, Chromotek); Species- and/or mouse isotype–specific secondary antibodies from donkey or goat conjugated to Alexa Fluor 488, Alexa Fluor 594, or Alexa Fluor 640 used for IFM or to Alexa Fluor 680 or Alexa Fluor 790 for immunoblots were obtained from Jackson ImmunoResearch Laboratories.

DNA constructs

All oligonucleotides used in constructing shRNA and expression plasmids are documented in Supplementary Table 1.

The pLKO.1-puromycin derived lentiviral vectors for small hairpin RNAs (shRNAs) against mouse PI4KIIα (shPI4KIIα-1, shPI4KIIα-2), PI4KIIβ (shPI4KIIβ-1, shPI4KIIβ-2), pallidin (shPallidin-1, shPallidin-2) and non-target control (shNC) were obtained from the High-throughput Screening Core of the University of Pennsylvania (Supplementary Table1). The plasmid-based expression vectors pEGFP-N1-PI4KIIα (Balla et al., 2002), pEGFP-N1-PI4KIIβ (Balla et al., 2002), pEGFP-C1-P4C-SidC (Dolinsky et al., 2014; Weber et al., 2018; Weber et al., 2014), pEGFP-C1-P4M-SidMx2 (Hammond et al., 2014), pEGFP-C1-VAMP7 (Dennis et al., 2016), pmCherry-STX13 (Dennis et al., 2016; Dennis et al., 2015), and pCR-OCA2-WT-HA-UTR2 (Sitaram et al., 2009) and the retroviral expression vector pBMN-mCherry-STX13-IRES-Hygro (X/N) (Bowman et al., 2021) have been previously described. Lentiviral packaging plasmid psPAX2 and pMD2.G encoding the vesicular stomatitis virus glycoprotein were gifts from Didier Trono (Univ. of Geneva) and purchased from Addgene (http://n2t.net/addgene:12260 and http://n2t.net/addgene:12259, respectively). Plasmids pBMN-GFP-P4C-SidC and pBMN-GFP-P4M-SidMx2 were generated by amplifying GFP-P4C-SidC and GFP-P4M-SidMx2 from pEGFP-C1-P4C-SidC and pEGFP-C1-P4M-SidMx2, respectively, using primers 1 and 2 for GFP-P4C-SidC and primers 1 and 3 for GFP-P4M-SidMx2. The amplified fragments were subcloned into the NotI restriction site of pBMN-IRES-hygro(X/N) (Setty et al., 2007), and the proper orientation of inserts was determined by gene amplification. The shRNA-resistant (shPI4KIIα-1^{R}) forms of PI4KIIα-WT-GFP, PI4KIIα-D308A-GFP and PI4KIIα-L61, 62A-GFP were generated by two-step gene amplification using the previously described MiGR-PI4KIIα-WT-GFP, MiGR-PI4KIIα-D308A-GFP and MiGR-PI4KIIα-L61, 62A-GFP, respectively, as templates (López-Haber et al., 2020). In the first step, fragments containing PI4KIIα cDNA 1-477 and PI4KIIα cDNA 459-1437 fused to GFP were separately amplified using primers 4 and 5 and primers 6 and 7, respectively. The two PCR products contain a 19-bp region of overlap containing the shPI4KIIα-1^{R} sequence CAAaAATGAgGAaCCCTAT

(mutagenized sites in small caps). The second step amplification concatenated the two PCR products using primers 4 and 7 to generate the full-length products, which were then subcloned into the NotI restriction site of pBMN-IRES-hygro(X/N) to generate pBMN-PI4KIIα-WT-GFP, pBMN-PI4KIIα-D308A-GFP and pBMN-PI4KIIα-L61, 62A-GFP. Similarly, the shRNA-resistant (shPI4KIIβ-2^{R}) forms of PI4KIIβ-WT-GFP and PI4KIIβ-D304A-GFP were generated by two-step amplification using pEGFP-N1-PI4KIIβ-WT and pEGFP-N1-PI4KIIβ-D304A (Balla et al., 2002) as templates, respectively. In the first step, fragments containing PI4KIIβ cDNA bp 1-1080 and PI4KIIβ bp cDNA 1063-1443 fused to GFP were separately amplified using primers 8 and 9 and primers 10 and 7, respectively. The two PCR products contain an 18-bp region of overlap containing the shPI4KIIβ-2^{R} sequence GAcGAgTGGAGAGCtTAT (mutagenized sites in small caps). The second step amplification concatenated the two PCR products using primers 8 and 7 to generate the full-length products, which were then subcloned into the NotI restriction site of pBMN-IRES-hygro(X/N) to generate pBMN-PI4KIIβ-WT-GFP and pBMN-PI4KIIβ-D308A-GFP. In all cases, the proper orientation of inserts within the pBMN-IRES-hygro vector was determined by gene amplification. The shPI4KIIβ-2^{R} form of pBMN-PI4KIIβ-L29, 30A-GFP was made by Gibson assembly using pBMN-PI4KIIβ-WT-GFP as template. Fragments containing PI4KIIβ cDNA bp 1-1017 and cDNA bp 987-1443 fused to GFP were amplified using primers 11 and 12, and primers 13 and 14, respectively. The two PCR products contain a 28-bp region of overlap GAGCC**GgcGgc**ACCGCGGATCGCCTGGG in which the codons for the two leucines of the AP-1 binding site are mutagenized to alanine codons (**alanine codons** in bold).

Cell culture and cell line generation

Immortalized melanocyte cell lines melan-Ink4a-1 (referred to here as melan-Ink4a or WT) derived from C57BL/6J-*Ink4a-Arf*$^{-/-}$ *(Cdk2a*-null*)* mice (Sviderskaya et al., 2002) and melan-pa1 (referred to here as melan-pa) derived from Pldn/BLOC-1-deficient C57BL/6J-*Pldn*$^{pa/pa}$ pallid mice (Setty et al., 2007) have been described. All melanocyte cell lines were cultured at 37°C and 10%

CO_2 in RPMI 1640 supplemented with 10% FBS (Atlanta Biologicals), 2 mM L-glutamine and 200 nM 12-*O*-tetradecanoylphorbol-13-acetate. Plat-E cells (Morita et al., 2000) were cultured at 37°C and 5% CO_2 in DMEM supplemented with 10% FBS (Hyclone), 2 mM L-glutamine, 1 mM sodium pyruvate with 1 µg/mL puromycin and 10 µg/mL blasticidin to maintain selection for the murine leukemia virus Gag and Env genes. HEK293T cells were cultured at 37°C and 5% CO_2 in DMEM supplemented with 10% FBS (Hyclone), 2 mM L-glutamine. All cell lines were tested to be negative for mycoplasma every 2–3 months using the MycoAlert Mycoplasma Detection Kit (Lonza).

Stable melan-Ink4a lines expressing mCherry-tagged STX13, GFP-P4C-SidC, or GFP-P4M-SidMx2 were generated by transducing melan-Ink4a cells with recombinant retroviruses encoding the indicated genes. Retroviruses were produced by Plat-E cells that were transiently transfected with indicated retroviral DNA constructs in the pBMN-IRES-hygro vector. Briefly, Plat-E cells were plated at 1.5×10^6 cells per 35-mm well and transfected the next day with 3.5 µg plasmid DNA using Lipofectamine 2000 (Thermo Fisher) in DMEM-containing medium according to manufacturer's instructions. The medium was replaced with RPMI 1640/ 10% FBS after 4-6 h, and retrovirus-containing supernatants were collected 48 h later, filtered, and added to melan-Ink4a cells seeded the previous day ($3\text{-}4 \times 10^5$ cells per 35-mm well). The retrovirus-containing supernatants was replaced with fresh medium containing 400-500 µg/ml hygromycin B, and polyclonal drug-resistant lines were selected over 14 d. Stable transfectant lines were occasionally treated with 200 µg/ml hygromycin B for 2–3 d to maintain selective pressure for the transgene.

Lentiviruses encoding shRNAs were harvested from transfected HEK293T cells that were co-transfected with packaging plasmid psPAX2, envelope plasmid pMD2.G, and pLKO.1 lentiviral plasmid containing the indicated shRNA insert and puromycin-resistance gene. HEK293T cells

plated at $1.5x10^6$ cells per 35-mm well the day before were transfected with 3.5 µg pLKO.1-shRNA, 2.625 µg psPAX2, and 0.875 µg pMD2.G using Lipofectamine 2000 (Thermo Fisher) according to the manufacturer's instructions. Medium replacement and virus harvesting were as described above for retroviral production. The lentivirus-containing supernatants were diluted 1:1 with fresh medium and added to melanocytes seeded the previous day ($3\text{-}4x10^5$ cells per 35-mm well). Transduced cells were selected using 2 µg/mL puromycin for 7-14 d or as indicated otherwise.

For transient transfection of melanocytes, cells were plated at $2.5\text{-}3x10^6$ cells per 35-mm well on Matrigel (BD)-coated coverslips (for OCA2-HA, GFP-VAMP7) or 35-mm glass-bottomed dishes (Matsunami D35-14-1.5-U; for mCherry-STX13, GFP-P4C, PI4KIIα-GFP, PI4KIIβ-GFP) and then transfected the next day with 1 µg (GFP-P4C) or 2 µg (OCA2-HA, GFP-VAMP7, mCherry-STX13, PI4KIIα-GFP, PI4KIIβ-GFP) of expression plasmid using Lipofectamine 3000 according to the manufacturer's instructions. Cells were imaged 24 h (GFP-VAMP7, GFP-P4C, PI4KIIα-GFP, PI4KIIβ-GFP) or 48 h (OCA2-HA, mCherry-STX13) after transfection.

Melanin content quantification

Quantification of melanin content by spectroscopy was performed essentially as described (Delevoye et al., 2009). Briefly, $1.2x10^6$ cells were seeded in 6-cm dishes in triplicate. The next day, cells were rinsed twice with PBS, detached by incubation in PBS, 10 mM EDTA for 15-20, and collected by centrifugation at 500 x *g* for 5 min. Cells were resuspended in cold 50 mM Tris-HCl, pH 7.4, 2 mM EDTA, 150 mM NaCl, 1 mM DTT, and 1x protease inhibitor cocktail (Roche), and then sonicated on ice using the Sonic Dismembrator Model 100 (Fisher Scientific). Sonicates were fractionated into supernatant and pellet fractions by centrifugation at 20,000 x *g* for 15 min at 4°C. Supernatants were subjected to determination of protein concentration by BCA protein determination kit (Thermo Fisher). Melanin-containing pellets were rinsed in ethanol/diethyl ether (1:1) and dissolved in 2 M NaOH/ 20% dimethyl sulfoxide at 60°C for 1 hour. The melanin content

of individual samples was measured by spectrophotometry as absorbance at 492 nm, and normalized to protein concentration in each sample. Triplicate samples were analyzed for each experimental condition in each experiment.

Immunoblotting

Melanocytes were cultured in 10-cm dishes, detached by incubation in PBS, 10 mM EDTA for 15-20 min, and collected by centrifugation at 500 x *g* for 5 min. Cell pellets were resuspended in cold 50 mM Tris-HCl, pH 7.4, 2 mM EDTA, 150 mM NaCl, 1 mM DTT, and 1x protease inhibitor cocktail (Roche), and lysed by sonication on ice using the Sonic Dismembrator Model 100 (Fisher Scientific). Concentrated Laemmli sample buffer with 2-mercaptoethanol was added to cell lysates and heated at 95-100°C for 10 min. Samples were then fractionated by 12% sodium dodecyl sulfate (SDS)/polyacrylamide gel electrophoresis (PAGE) on polyacrylamide gels and transferred to polyvinylidene difluoride membranes (Immobilon-FL, Millipore). Membranes were blocked with Odyssey Blocking Buffer at room temperature (RT) for 1 h, incubated with primary antibody diluted in TBS/ 0.2% tween-20 (TBST) overnight at 4°C, washed 3 times 10 min with TBST, and then incubated with secondary antibody conjugated with either Alexa Fluor 680 or Alexa Fluor 790, diluted in TBST, at RT for 1 h. After washing 3 times 10 min with TBST, blots were analyzed using a LI-COR Odyssey CLx imaging system, and images were further processed and quantified using Fiji-ImageJ (National Institutes of Health).

Subcellular fractionation

Subcellular fractionation was performed essentially as described (Di Pietro et al., 2004; Di Pietro et al., 2006) with minor modifications. All steps were performed at 4°C. To prepare cytosolic and membrane fractions, melanocytes were homogenized at 10^7 cells/ml in hypotonic buffer [10 mM HEPES, pH 7.4, 1 mM $MgCl_2$, 1 mM EGTA, 250 mM sucrose, 2 mM DTT, 1x protease inhibitor cocktail (Roche), 1x phosphatase inhibitor (Roche)] by passing cells through a pre-chilled 28G

needle for 25-30 cycles until 70-80% cells were disrupted as evaluated by trypan blue exclusion. Undisrupted cells in the crude homogenate were pelleted by centrifugation at 500 x *g* for 1 min, and the supernatant was then centrifuged at 5000 x *g* for 10 min to remove nuclei and mitochondria. The resulting post-nuclear supernatant was fractionated into membrane pellet and cytosolic supernatant fractions by centrifugation at 100,000 x *g* for 60 min. Membrane pellets were gently washed once in hypotonic buffer to minimize contamination by cytosolic proteins and then solubilized in hypotonic buffer containing 0.2% SDS to the same volume as the cytosol fraction. 6X Laemmli sample buffer with 2-mercaptoethanol was added to solubilized membrane and cytosolic fractions (to a final 1X concentration), and samples were heated at 95-100°C for 10 min. Identical volumes of membrane and cytosolic fractions were fractionated by SDS-PAGE on 12% polyacrylamide gels and analyzed by immunoblotting.

Immunofluorescence microscopy and live-cell imaging

Immunofluorescence microscopy was performed essentially as described (Bowman et al., 2021; Dennis et al., 2016). Briefly, melanocytes were seeded on matrigel-coated coverslips 24-48 h before fixation. Cells were fixed with 4% formaldehyde (VWR Scientific) in PBS (RT, 15 min), washed 5 times with PBS, incubated with primary antibody (RT, 1 h) diluted in blocking buffer (0.01% BSA and 0.02% Saponin in PBS), washed 3 times 5 min with PBS, incubated with secondary antibodies (RT, 30 min) diluted in blocking buffer, washed again, and mounted onto slides using Prolong Gold (Thermo Fisher). Fixed cell images were acquired using a Leica DMI8 inverted microscope (Leica Biosystems) equipped with a CSU-WI spinning-disk confocal scanner unit (Yokogawa), a 100X total internal reflection fluorescence objective (1.47NA), a Hamamatsu Photonics ORCA-Flash 4.0 sCMOS digital camera, and VisiView software (Visitron System). Images were further processed and analyzed using Fiji-ImageJ.

Live-cell imaging was done essentially as described (Bowman et al., 2021). Briefly, melanocytes were seeded onto matrigel-coated 35-mm glass-bottomed dishes, incubated in Leibovitz's CO_2-independent medium without phenol red (Invitrogen) supplemented with 10% FBS in an environmental chamber set to 37°C, and imaged using the same microscopic system. To image tubule dynamics, z-series images spanning two to five 0.2-μm layers were captured every 0.6–1 s for a minimum of 30 s and a maximum of 90 s. To observe cellular PtdIns4P distribution, sixteen 0.2-μm layers of z-series were acquired for further analysis. Dual-view live-cell imaging was performed using the Hamamatsu W-VIEW GEMINI Image splitting optics, and one to three 0.2-μm layers of z-series were captured every 0.4-0.5 s for a minimum of 20 s and a maximum of 80 s.

Quantitative image Analysis

Colocalization analyses. The area of overlap between fluorescently labeled proteins and pigmented melanosomes or between two fluorescently labeled proteins was quantified using Fiji-ImageJ on fixed cell images essentially as previously described (Bowman et al., 2021; Dennis et al., 2015). Briefly, single z-plane images were cropped around single cells, and the nucleus and densely labeled perinuclear region were removed. The local background of fluorescent images was subtracted using the "rolling ball" algorithm with "sliding paraboloid" selected; the rolling ball radius was chosen based on fluorescence intensity, such that a smaller radius was used for higher fluorescence intensity values (e.g. 2 pixels for most TYRP1, STX13, LAMP2, and OCA2-HA images) and a higher radius for lower intensity values (e.g. 10 pixels for GFP-VAMP7). Pigment granules from the bright field channel were processed using the "Invert" function. After background subtraction, images were converted to binary images using either the "Threshold" function (TYRP1, STX13, LAMP2 and OCA2-HA) or the Bernson algorithm of the "Auto Local Threshold" function with a 15 pixel radius (GFP-VAMP7), and structures of less than 5 pixels in area were considered background and filtered out. To generate an overlap image, two binary

images were multiplied using the “Image Calculator” function, and the areas of the individual and overlap binary images were calculated using the “Analyze Particles” function. Percentage of overlap was calculated as the percentage of the area of overlap relative to the area of one of the individual labels.

P4M labeling analyses. To assess the degree to which the PtdIns4P probe GFP-P4M-SidMx2 (P4M) localized to punctate structures in stably transfected melan-Ink4a mouse melanocytes, we analyzed the degree of variation in signal intensity across individual cells. This was based on the notion that the intensity of the signal from cytoplasmic- and/or plasma membrane-localized P4M does not vary largely across the cell, whereas the signal from endolysosomes or other punctate structures will show substantial variation across the field. To assess signal variation, first a maximum-intensity projection was generated from seven consecutive 0.2-μm z layers of a z-series from chosen fields, and fifteen cytoplasmic 25-μm^2 square regions were randomly selected within each cell for single cell analysis. For background subtraction, an average value was calculated from the mean fluorescence intensity of several 25-μm^2 square regions in the field that lacked any cells, and this value was subtracted from the value of the positive regions. The mean fluorescence intensity and standard deviation (SD) of each 25-μm^2 square region were acquired using the “Measure” function in Fiji-ImageJ. Because the expression level of P4M varied from cell to cell and cells with higher P4M levels will tend toward higher SDs, the SD was normalized to a “coefficient of variation” using the following formula: Coefficient of Variation = (Standard Deviation / Mean) x 100. In the graphs shown in **Fig. S4B and C**, a single dot indicates the average SD or coefficient of variation value, respectively, from fifteen 25-μm^2 regions within a single cell.

Number and percentage of PtdIns4P-containing tubules. Quantification of tubules containing PtdIns4P, as labeled by the GFP-P4C-SidC (P4C) probe, was done using Fiji-ImageJ on video streams of melan-Ink4a mouse melanocytes that stably express P4C and transiently express

mCherry-STX13 (STX13). A maximum-intensity projection was generated from three consecutive 0.2-μm z layers of a z-series from a single frame of a video stream, and two cytoplasmic 100-μm^2 square regions were randomly selected for a single cell analysis. Background subtraction and segmentation of both P4C and STX13 were processed using the Squassh algorithm (Rizk et al., 2014) with the following parameters: rolling ball window size of 20 pixels in the Background subtractor; 0.04 for minimum object intensity channel; "Subpixel segmentation" selected; and 0.4 for standard deviation of xy and z in the PSF model. Binary images were generated using the "Squassh"ed algorithm, and structures in which binary P4C- and STX13-containing structures overlapped were visualized using the "Image Calculator" "multiply" function. Circular structures in binary images were removed and tubular structures were quantified using the Analyze particles function with size of 0.0625 μm^2-infinity and circularity of 0-0.7. In the graphs shown in **Fig. 8B-D**, a single dot indicates the average of two 100-μm^2 regions within a single cell.

Number, percentage, and length of STX13-containing tubules. Quantification of endosomal tubules labeled by mCherry-STX13 was performed using Fiji-ImageJ on melan-Ink4a mouse melanocytes that stably express mCherry-STX13. Single plane images with largely in-focus STX13-positive structures were selected from image sequences, and ten cytoplasmic 25-μm^2 square regions were randomly chosen and analyzed individually. Signal background was subtracted using the the Rolling Ball algorithm with a 10 pixel radius and Sliding Paraboloid selected. After background subtraction, images were processed by Smooth to reduce noise and then rendered binary using the Phansalkar algorithm of the "Auto Local Threshold" function with a 15 pixel radius, followed by the Skeletonize function. The Analyze Skeleton function was used to calculate and document the length and number of tubules, represented as Branches. Only branches longer than 0.25 μm were considered as tubules. Tubule length was determined by averaging all branches longer than 0.25 μm within each 25-μm^2 region of a single cell. In the

graphs shown in **Fig. 9D-G**, a single dot represents the average of ten 25-μm^2 regions within a single cell.

Statistical analysis

Except where specified, at least three independent replicates were performed in each experiment and sample sizes are as indicated in each figure legend. Statistical results were presented as mean ± SD. Statistical analyses were performed in GraphPad Prism using ordinary one-way ANOVA, Welsh's ANOVA, or Kruskal-Wallis test with post-hoc correction as specified and determined using GraphPad Prism by assessing each data set for normality and homoscedasticity; Welsh's ANOVA was used when the data set did not display homoscedasticity, and a Kruskal-Wallis test was used if the data set did not display a normal distribution. Significance between control or experimental samples are indicated; only $p < 0.05$ was considered as statistically significant.

ACKNOWLEDGMENTS

We are extremely grateful to Tamas Balla, Sergio Grinstein, and Christopher Burd for PI4KIIα and PI4KIIβ molecular reagents and the P4C and 2XP4M probes and helpful discussions, Pietro De Camilli for antibodies specific for PI4KIIα and PI4KIIβ, Juan Bonifacino for the rabbit antibody to pallidin, Rytis Prekeris for the rabbit antibody to STX13, Shanna Bowman and Linh Le for advice on video microscopy and image quantification, and Dawn Harper for laboratory assistance. We are grateful for funding from National Institutes of Health grants R01-EY015625 from the National Eye Institute (to MSM and GR), Institut National de la Santé et de la Recherche Médicale (to CD), Centre National de la Recherche Scientifique (to GR), Institut Curie (to GR and CD), and Genespoir (to CD).

AUTHOR CONTRIBUTIONS

All authors edited the manuscript. In addition:

Yueyao Zhu contributed to conceptualization of the project and experimental design, performed most of the experiments, analyzed the data, assembled the figures, wrote the original draft of the paper, and finalized editing of the manuscript with Michael Marks.

Shuixing Li contributed to experimental design and performed some of the experiments.

Alexa Jaume contributed to experimental design, performed some of the experiments, and analyzed the data for these experiments.

Riddhi Atul Jani, Cédric Delevoye, and Graça Raposo contributed to conceptualization of the project, experimental design, and data interpretation.

Michael S. Marks contributed to conceptualization of the project, supervised and administered the project, coordinated among all contributors, provided resources, analyzed data, edited figures, wrote part of the original manuscript draft, and coordinated editing by all co-authors.

REFERENCES

Balla, A., and T. Balla. 2006. Phosphatidylinositol 4-kinases: old enzymes with emerging functions. *Trends Cell Biol*. 16:351-361.

Balla, A., G. Tuymetova, M. Barshishat, M. Geiszt, and T. Balla. 2002. Characterization of type II phosphatidylinositol 4-kinase isoforms reveals association of the enzymes with endosomal vesicular compartments. *J Biol Chem*. 277:20041-20050.

Balla, T. 2013. Phosphoinositides: tiny lipids with giant impact on cell regulation. *Physiol. Rev.* 93:1019-1137.

Bellono, N.W., and E.V. Oancea. 2014. Ion transport in pigmentation. *Arch Biochem Biophys*. 563:35-41.

Bowman, S.L., J. Bi-Karchin, L. Le, and M.S. Marks. 2019. The road to LROs: insights into lysosome-related organelles from Hermansky-Pudlak syndrome and other rare diseases. *Traffic*. 20:404-435.

Bowman, S.L., L. Le, Y. Zhu, D.C. Harper, A. Sitaram, A.C. Theos, E.V. Sviderskaya, D.C. Bennett, G. Raposo, D.J. Owen, M.K. Dennis, and M.S. Marks. 2021. A BLOC-1-AP-3 super-complex sorts a cis-SNARE complex into endosome-derived tubular transport carriers. *J. Cell Biol.* 220:e202005173.

Burgess, J., L.M. Del Bel, C.I. Ma, B. Barylko, G. Polevoy, J. Rollins, J.P. Albanesi, H. Krämer, and J.A. Brill. 2012. Type II phosphatidylinositol 4-kinase regulates trafficking of secretory granule proteins in Drosophila. *Development*. 139:3040-3050.

Campagne, C., L. Ripoll, F. Gilles-Marsens, G. Raposo, and C. Delevoye. 2018. AP-1/KIF13A blocking peptides impair melanosome maturation and melanin synthesis. *Int. J. Mol. Sci.* 19:568.

Craige, B., G. Salazar, and V. Faundez. 2008. Phosphatidylinositol-4-kinase type II alpha contains an AP-3 sorting motif and a kinase domain that are both required for endosome traffic. *Mol. Biol. Cell*. 19:1415-1426.

D'Angelo, G., M. Vicinanza, A. Di Campli, and M.A. De Matteis. 2008. The multiple roles of PtdIns(4)P -- not just the precursor of PtdIns(4,5)P2. *J. Cell Sci.* 121:1955-1963.

De Jesus Rojas, W., and L.R. Young. 2020. Hermansky-Pudlak Syndrome. *Semin. Respir. Crit. Care Med.* 41:238-246.

Delevoye, C., X. Heiligenstein, L. Ripoll, F. Gilles-Marsens, M.K. Dennis, R.A. Linares, L. Derman, A. Gokhale, E. Morel, V. Faundez, M.S. Marks, and G. Raposo. 2016. BLOC-1

brings together the actin and microtubule cytoskeletons to generate recycling endosomes. *Curr. Biol.* 26:1-13.

Delevoye, C., I. Hurbain, D. Tenza, J.-B. Sibarita, S. Uzan-Gafsou, H. Ohno, W.J.C. Geerts, A.J. Verkleij, J. Salamero, M.S. Marks, and G. Raposo. 2009. AP-1 and KIF13A coordinate endosomal sorting and positioning during melanosome biogenesis. *J. Cell Biol.* 187:247-264.

Delevoye, C., M.S. Marks, and G. Raposo. 2019. Lysosome-related organelles as functional adaptations of the endolysosomal system. *Curr Opin Cell Biol*. 59:147-158.

Delevoye, C., S. Miserey-Lenkei, G. Montagnac, F. Gilles-Marsens, P. Paul-Gilloteaux, F. Giordano, F. Waharte, M.S. Marks, B. Goud, and G. Raposo. 2014. Recycling endosome tubule morphogenesis from sorting endosomes requires the kinesin motor KIF13A. *Cell Rep.* 6:445-454.

Dennis, M.K., C. Delevoye, A. Acosta-Ruiz, I. Hurbain, M. Romao, G.G. Hesketh, P.S. Goff, E.V. Sviderskaya, D.C. Bennett, J.P. Luzio, T. Galli, D.J. Owen, G. Raposo, and M.S. Marks. 2016. BLOC-1 and BLOC-3 regulate VAMP7 cycling to and from melanosomes via distinct tubular transport carriers. *J. Cell Biol.* 214:293-308.

Dennis, M.K., A.R. Mantegazza, O.L. Snir, D. Tenza, A. Acosta-Ruiz, C. Délevoye, R. Zorger, A. Sitaram, W. de Jesus-Rojas, K. Ravichandran, J. Rux, E.V. Sviderskaya, D.C. Bennett, R. G., M.S. Marks, and S.R.G. Setty. 2015. BLOC-2 targets recycling endosomal tubules to melanosomes for cargo delivery. *J. Cell Biol.* 209:563-577.

Di Pietro, S.M., and E.C. Dell'Angelica. 2005. The cell biology of Hermansky-Pudlak syndrome: recent advances. *Traffic*. 6:525-533.

Di Pietro, S.M., J.M. Falcon-Perez, and E.C. Dell'Angelica. 2004. Characterization of BLOC-2, a complex containing the Hermansky-Pudlak syndrome proteins HPS3, HPS5 and HPS6. *Traffic*. 5:276-283.

Di Pietro, S.M., J.M. Falcon-Perez, D. Tenza, S.R.G. Setty, M.S. Marks, G. Raposo, and E.C. Dell'Angelica. 2006. BLOC-1 interacts with BLOC-2 and the AP-3 complex to facilitate protein trafficking on endosomes. *Mol. Biol. Cell*. 17:4027-4038.

Dolinsky, S., I. Haneburger, A. Cichy, M. Hannemann, A. Itzen, and H. Hilbi. 2014. The Legionella longbeachae Icm/Dot substrate SidC selectively binds phosphatidylinositol 4-phosphate with nanomolar affinity and promotes pathogen vacuole-endoplasmic reticulum interactions. *Infect. Immun.* 82:4021-4033.

Domingues, L., A. Ismail, N. Charro, I. Rodriguez-Escudero, D.W. Holden, M. Molina, V.J. Cid, and L.J. Mota. 2016. The Salmonella effector SteA binds phosphatidylinositol 4-phosphate for subcellular targeting within host cells. *Cell. Microbiol.* 18:949-969.

Dong, R., Y. Saheki, S. Swarup, L. Lucast, J.W. Harper, and P. De Camilli. 2016. Endosome-ER contacts control actin nucleation and retromer function through VAP-dependent regulation of PI4P. *Cell*. 166:408-423.

Du, W., Q.P. Su, Y. Chen, Y. Zhu, D. Jiang, Y. Rong, S. Zhang, Y. Zhang, H. Ren, C. Zhang, X. Wang, N. Gao, Y. Wang, L. Sun, Y. Sun, and L. Yu. 2016. Kinesin 1 drives autolysosome tubulation. *Dev. Cell*. 37:326-336.

Gokhale, A., J. Larimore, E. Werner, L. So, A. Moreno-De-Luca, C. Lese-Martin, V.V. Lupashin, Y. Smith, and V. Faundez. 2012. Quantitative proteomic and genetic analyses of the schizophrenia susceptibility factor dysbindin identify novel roles of the biogenesis of lysosome-related organelles complex 1. *J. Neurosci.* 32:3697-3711.

Graham, T.R., and C.G. Burd. 2011. Coordination of Golgi functions by phosphatidylinositol 4-kinases. *Trends Cell Biol.* 21:113-121.

Guo, J., M.R. Wenk, L. Pellegrini, F. Onofri, F. Benfenati, and P. De Camilli. 2003. Phosphatidylinositol 4-kinase type IIalpha is responsible for the phosphatidylinositol 4-kinase activity associated with synaptic vesicles. *Proc Natl Acad Sci U S A*. 100:3995-4000.

Hammond, G.R., M.P. Machner, and T. Balla. 2014. A novel probe for phosphatidylinositol 4-phosphate reveals multiple pools beyond the Golgi. *J. Cell Biol.* 205:113-126.

Highland, C.M., and J.C. Fromme. 2021. Arf1 directly recruits the Pik1-Frq1 PI4K complex to regulate the final stages of Golgi maturation. *Mol. Biol. Cell*. 32:1064-1080.

Huotari, J., and A. Helenius. 2011. Endosome maturation. *EMBO J.* 30:3481-3500.

Jani, R.A., A. Di Cicco, T. Keren-Kaplan, S. Vale-Costa, D. Hamaoui, I. Hurbain, F.-C. Tsai, M. Dimarco, A.-S. Macé, Y. Zhu, M.J. Amorim, P. Bassereau, J.S. Bonifacino, A. Subtil, M.S. Marks, D. Levy, G. Raposo, and C. Delevoye. 2021. Phosphatidylinositol-4-phosphate initiates endosomal membrane remodeling through BLOC-1-dependent tubule formation. *J. Cell Biol.* Submitted.

Jovic, M., M.J. Kean, A. Dubankova, E. Boura, A.C. Gingras, J.A. Brill, and T. Balla. 2014. Endosomal sorting of VAMP3 is regulated by PI4K2A. *J. Cell Sci.* 127:3745-3756.

Jovic, M., F. Kieken, N. Naslavsky, P.L. Sorgen, and S. Caplan. 2009. Eps15 homology domain 1-associated tubules contain phosphatidylinositol-4-phosphate and phosphatidylinositol-(4,5)-bisphosphate and are required for efficient recycling. *Mol. Biol. Cell*. 20:2731-2743.

Kinosita, K., Jr., H. Itoh, S. Ishiwata, K. Hirano, T. Nishizaka, and T. Hayakawa. 1991. Dual-view microscopy with a single camera: real-time imaging of molecular orientations and calcium. *J. Cell Biol.* 115:67-73.

Kitamata, M., T. Inaba, and S. Suetsugu. 2020. The roles of the diversity of amphipathic lipids in shaping membranes by membrane-shaping proteins. *Biochem. Soc. Trans.* 48:837-851.

Klopfenstein, D.R., M. Tomishige, N. Stuurman, and R.D. Vale. 2002. Role of phosphatidylinositol(4,5)bisphosphate organization in membrane transport by the Unc104 kinesin motor. *Cell*. 109:347-358.

Klumperman, J., and G. Raposo. 2014. The complex ultrastructure of the endolysosomal system. *Cold Spring Harb. Perspect. Biol.* 6:a016857.

Larimore, J., K. Tornieri, P.V. Ryder, A. Gokhale, S.A. Zlatic, B. Craige, J.D. Lee, K. Talbot, J.-F. Pare, Y. Smith, and V. Faundez. 2011. The schizophrenia susceptibility factor dysbindin and its associated complex sort cargoes from cell bodies to the synapse. *Mol. Biol. Cell*. 22:4854-4867.

Le, L., J. Sires-Campos, G. Raposo, C. Delevoye, and M.S. Marks. 2021. Melanosome biogenesis in the pigmentation of mammalian skin. *Integr. Comp. Biol.* 61:1517-1545.

Lee, H.H., D. Nemecek, C. Schindler, W.J. Smith, R. Ghirlando, A.C. Steven, J.S. Bonifacino, and J.H. Hurley. 2012. Assembly and architecture of Biogenesis of Lysosome-related Organelles Complex-1 (BLOC-1). *J. Biol. Chem.* 287:5882-5890.

Levin-Konigsberg, R., F. Montaño-Rendón, T. Keren-Kaplan, R. Li, B. Ego, S. Mylvaganam, J.E. DiCiccio, W.S. Trimble, M.C. Bassik, J.S. Bonifacino, G.D. Fairn, and S. Grinstein. 2019. Phagolysosome resolution requires contacts with the endoplasmic reticulum and phosphatidylinositol-4-phosphate signalling. *Nature Cell Biology*. 21:1234-1247.

Lopes da Silva, M., and D.F. Cutler. 2016. von Willebrand factor multimerization and the polarity of secretory pathways in endothelial cells. *Blood*. 128:277-285.

López-Haber, C., R. Levin-Konigsberg, Y. Zhu, J. Bi-Karchin, T. Ball, S. Grinstein, M.S. Marks, and A.R. Mantegazza. 2020. Phosphatidylinositol-4-kinase IIα licenses phagosomes for TLR4 signaling and MHC-II presentation in dendritic cells. *Proc. Natl. Acad. Sci. U.S.A.* 117:28251-28262.

Ma, C.-I.J., Y. Yang, T. Kim, C.H. Chen, G. Polevoy, M. Vissa, J. Burgess, and J.A. Brill. 2020. An early endosome–derived retrograde trafficking pathway promotes secretory granule maturation. *Journal of Cell Biology*. 219:e201808017.

Mani, M., U.H. Lee, N.A. Yoon, E.H. Yoon, B.J. Lee, W.J. Cho, and J.W. Park. 2017. Developmentally regulated GTP-binding protein 2 is required for stabilization of Rac1-positive membrane tubules. *Biochem. Biophys. Res. Commun.* 493:758-764.

Mantegazza, A.R., A.L. Zajac, A. Twelvetrees, E.L.F. Holzbaur, S. Amigorena, and M.S. Marks. 2014. TLR-dependent phagosome tubulation in dendritic cells promotes phagosome cross-talk to optimize MHC-II antigen presentation. *Proc. Natl. Acad. Sci. U.S.A.* 111:15508-15513.

McGrath, M.J., M.J. Eramo, R. Gurung, A. Sriratana, S.M. Gehrig, G.S. Lynch, S.R. Lourdes, F. Koentgen, S.J. Feeney, M. Lazarou, C.A. McLean, and C.A. Mitchell. 2021. Defective lysosome reformation during autophagy causes skeletal muscle disease. *J. Clin. Invest.* 131:e135124.

Minogue, S. 2018. The many roles of type II phosphatidylinositol 4-kinases in membrane trafficking: new tricks for old dogs. *Bioessays*. 40:1700145.

Morita, S., T. Kojima, and T. Kitamura. 2000. Plat-E: an efficient and stable system for transient packaging of retroviruses. *Gene Ther.* 7:1063-1066.

Moriyama, K., and J.S. Bonifacino. 2002. Pallidin is a component of a multi-protein complex involved in the biogenesis of lysosome-related organelles. *Traffic*. 3:666-677.

Nakagawa, T., M. Setou, D. Seog, K. Ogasawara, N. Dohmae, K. Takio, and N. Hirokawa. 2000. A novel motor, KIF13A, transports mannose-6-phosphate receptor to plasma membrane through direct interaction with AP-1 complex. *Cell*. 103:537-540.

Novikoff, A.B., A. Albala, and L. Biempica. 1968. Ultrastructural and cytochemical observations on B-16 and Harding-Passey mouse melanomas. The origin of premelanosomes and compound melanosomes. *J. Histochem. Cytochem.* 16:299-319.

Patwardhan, A., S. Bardin, S. Miserey-Lenkei, L. Larue, B. Goud, G. Raposo, and C. Delevoye. 2017. Routing of the RAB6 secretory pathway towards the lysosome related organelle of melanocytes. *Nat. Commun.* 8:15835.

Rahajeng, J., R.S. Kuna, S.L. Makowski, T.T.T. Tran, M.D. Buschman, S. Li, N. Cheng, M.M. Ng, and S.J. Field. 2019. Efficient Golgi forward trafficking requires GOLPH3-driven, PI4P-dependent membrane curvature. *Dev. Cell*. 50:573-585.

Raposo, G., D. Tenza, D.M. Murphy, J.F. Berson, and M.S. Marks. 2001. Distinct protein sorting and localization to premelanosomes, melanosomes, and lysosomes in pigmented melanocytic cells. *J. Cell Biol.* 152:809-823.

Rizk, A., G. Paul, P. Incardona, M. Bugarski, M. Mansouri, A. Niemann, U. Ziegler, P. Berger, and I.F. Sbalzarini. 2014. Segmentation and quantification of subcellular structures in fluorescence microscopy images using Squassh. *Nat Protoc*. 9:586-596.

Salazar, G., B. Craige, M.L. Styers, K.A. Newell-Litwa, M.M. Doucette, B.H. Wainer, J.M. Falcon-Perez, E.C. Dell'Angelica, A.A. Peden, E. E. Werner, and V. Faundez. 2006. BLOC-1 complex deficiency alters the targeting of Adaptor Protein complex-3 cargoes. *Mol. Biol. Cell*. 17:4014-4026.

Salazar, G., B. Craige, B.H. Wainer, J. Guo, P. De Camilli, and V. Faundez. 2005. Phosphatidylinositol-4-kinase type II a is a component of AP-3-derived vesicles. *Mol. Biol. Cell*. 16:3692-3704.

Salazar, G., S. Zlatic, B. Craige, A.A. Peden, J. Pohl, and V. Faundez. 2009. Hermansky-pudlak syndrome protein complexes associate with phosphatidylinositol-4-kinase type II alpha in neuronal and non-neuronal cells. *J. Biol. Chem.* 284:1790-1802.

Seiji, M., T.B. Fitzpatrick, and M.S.C. Birbeck. 1961. The melanosome: a distinctive subcellular particle of mammalian melanocytes and the site of melanogenesis. *J. Invest. Dermatol.* 36:243-252.

Setty, S.R.G., D. Tenza, E.V. Sviderskaya, D.C. Bennett, G. Raposo, and M.S. Marks. 2008. Cell-specific ATP7A transport sustains copper-dependent tyrosinase activity in melanosomes. *Nature*. 454:1142-1146.

Setty, S.R.G., D. Tenza, S.T. Truschel, E. Chou, E.V. Sviderskaya, A.C. Theos, M.L. Lamoreux, S.M. Di Pietro, M. Starcevic, D.C. Bennett, E.C. Dell'Angelica, G. Raposo, and M.S. Marks. 2007. BLOC-1 is required for cargo-specific sorting from vacuolar early endosomes toward lysosome-related organelles. *Mol. Biol. Cell*. 18:768-780.

Sitaram, A., M.K. Dennis, R. Chaudhuri, W. De Jesus-Rojas, D. Tenza, S.R.G. Setty, C.S. Wood, E.V. Sviderskaya, D.C. Bennett, G. Raposo, J.S. Bonifacino, and M.S. Marks. 2012. Differential recognition of a dileucine-based sorting signal by AP-1 and AP-3 reveals a requirement for both BLOC-1 and AP-3 in delivery of OCA2 to melanosomes. *Mol. Biol. Cell*. 23:3178-3192.

Sitaram, A., R. Piccirillo, I. Palmisano, D.C. Harper, E.C. Dell'Angelica, M.V. Schiaffino, and M.S. Marks. 2009. Localization to mature melanosomes by virtue of cytoplasmic dileucine motifs is required for human OCA2 function. *Mol. Biol. Cell*. 20:1464-1477.

Stalder, D., and D.C. Gershlick. 2020. Direct trafficking pathways from the Golgi apparatus to the plasma membrane. *Semin. Cell Dev. Biol.* 107:112-125.

Suetsugu, S., S. Kurisu, and T. Takenawa. 2014. Dynamic shaping of cellular membranes by phospholipids and membrane-deforming proteins. *Physiol. Rev.* 94:1219-1248.

Sviderskaya, E.V., S.P. Hill, T.J. Evans-Whipp, L. Chin, S.J. Orlow, D.J. Easty, S.C. Cheong, D. Beach, R.A. DePinho, and D.C. Bennett. 2002. p16Ink4a in melanocyte senescence and differentiation. *J. Natl. Cancer Inst.* 94:446-454.

Tamura, K., N. Ohbayashi, K. Ishibashi, and M. Fukuda. 2011. Structure-function analysis of VPS9-ankyrin-repeat protein (Varp) in the trafficking of tyrosinase-related protein 1 in melanocytes. *J. Biol. Chem.* 286:7507-7521.

Tan, J., and J.A. Brill. 2014. Cinderella story: PI4P goes from precursor to key signaling molecule. *Crit. Rev. Biochem. Mol. Biol.* 49:33-58.

Theos, A.C., D. Tenza, J.A. Martina, I. Hurbain, A.A. Peden, E.V. Sviderskaya, A. Stewart, M.S. Robinson, D.C. Bennett, D.F. Cutler, J.S. Bonifacino, M.S. Marks, and G. Raposo. 2005. Functions of AP-3 and AP-1 in tyrosinase sorting from endosomes to melanosomes. *Mol. Biol. Cell*. 16:5356-5372.

Vijayasaradhi, S., Y.Q. Xu , B. Bouchard, and A.N. Houghton. 1995. Intracellular sorting and targeting of melanosomal membrane proteins: identification of signals for sorting of the human brown locus protein, gp75. *J. Cell Biol.* 130:807-820.

Wang, Y.J., J. Wang, H.Q. Sun, M. Martinez, Y.X. Sun, E. Macia, T. Kirchhausen, J.P. Albanesi, M.G. Roth, and H.L. Yin. 2003. Phosphatidylinositol 4 phosphate regulates targeting of clathrin adaptor AP-1 complexes to the Golgi. *Cell*. 114:299-310.

Weber, S., B. Steiner, A. Welin, and H. Hilbi. 2018. Legionella-containing vacuoles capture PtdIns(4)P-rich vesicles derived from the Golgi apparatus. *mBio*. 9:e02420-02418.

Weber, S., M. Wagner, and H. Hilbi. 2014. Live-cell imaging of phosphoinositide dynamics and membrane architecture during Legionella infection. *mBio*. 5:e00839-00813.

Wieffer, M., E. Cibrian Uhalte, Y. Posor, C. Otten, K. Branz, I. Schutz, J. Mossinger, P. Schu, S. Abdelilah-Seyfried, M. Krauss, and V. Haucke. 2013. PI4K2beta/AP-1-based TGN-endosomal sorting regulates Wnt signaling. *Curr. Biol.* 23:2185-2190.

FIGURE LEGENDS

Figure 1. Depletion of either PI4KIIα or PI4KIIβ by shRNA in WT melanocytes impairs localization of BLOC-1-dependent cargoes to melanosomes.

WT melan-Ink4a melanocytes were transduced with lentiviruses expressing the indicated shRNAs to PI4KIIα, PI4KIIβ, the Pallidin subunit of BLOC-1, or control non-coding shRNA (shNC) and selected for 7-14 d. Cells in D, E were additionally transiently transfected to express HA-tagged OCA2 (OCA2-HA) 2 d prior to analysis. **(*A* and *D*)** 7 to 14 d after shRNA transduction, cells were analyzed by IFM for endogenous TYRP1 (A; green, left and right panels) or the HA-tagged transgene OCA2 (D; left and right panels), and by bright field microscopy (BF) for pigment granules (middle; pseudocolored magenta in the merged images on the right). White arrows, examples of pigment granules surrounded by TYRP1 or overlapping with OCA2-HA; yellow arrowheads, examples of mislocalized TYRP1 or OCA2-HA not associated with pigment granules. Boxed regions are magnified 5-fold in the insets. Scale bars: main panels, 10 μm; insets, 2 μm. **(*B, C and E*)** Quantification of the degree to which TYRP1 (B) or HA-OCA2 (E) overlap with melanosomes or to which melanosomes are coated with TYRP1 (C) in cells treated with the indicated shRNAs. Data are presented as a scatter plot in which individual cells are indicated by single dot colored to represent one of two (C) or three (B and E) independent experiments; means of each experiment are indicated by triangles, and the overall mean and SD are indicated by bars. Datasets were analyzed by either Kruskal-Wallis (B and C) or Welch's ANOVA test (E); ****, $p<0.0001$; NS, not significant. **(*F*)** WT Melan-Ink4a cells treated with the indicated shRNAs for 14 days or HEK293T cells as a negative control were analyzed by quantitative melanin content assay. Data are presented as mean ± SD of five independent experiments as a percentage of the signal from shNC-treated cells. Data were analyzed by Welch's ANOVA test relative to shNC-treated cells; ****, $p<0.0001$; *, $p<0.05$; NS, not significant.

Figure 2. TYRP1 is mislocalized to early endosomes and late endosomes/ lysosomes in WT melanocytes depleted of either PI4KIIα or PI4KIIβ.

WT melan-Ink4a melanocytes were transduced with lentiviruses expressing the indicated shRNAs to PI4KIIα, PI4KIIβ, or the Pallidin subunit of BLOC-1, or control non-coding shRNA (shNC) and selected for 7 to 14 d. **(*A* and *C*)** Cells were analyzed by IFM for endogenous TYRP1 (green, left and right panels) localization relative to STX13 to mark early endosomes (A) or LAMP2 to mark late endosomes and lysosomes (C) (magenta, middle and right panels). White arrows, examples of TYRP1 not associated with STX13 or LAMP2; yellow arrowheads, examples of TYRP1 overlapping with STX13 or LAMP2. Boxed regions are magnified 5-fold in the insets. Scale bars: main panels, 10 μm; insets, 2 μm. **(*B* and *D*)** Quantification of the degree of TYRP1 overlap with STX13 (B) or LAMP2 (D) in cells treated with the indicated shRNAs. Data are presented as a scatter plot in which individual cells are indicated by a single dot colored to represent one of three independent experiments; means of each experiment are indicated by triangles, and overall mean and SD are indicated by bars. Datasets were analyzed by ordinary one-way ANOVA (B) or Welch's ANOVA test (D); ****, $p<0.0001$; NS, not significant.

Figure 3. PI4KIIα function in TYRP1 trafficking requires its lipid kinase activity and binding to adaptor AP-3.

WT melan-Ink4a melanocytes were untransduced (A, B) or transduced with retroviruses encoding hygromycin resistance and GFP-tagged PI4KIIα-WT (C), kinase-dead mutant PI4KIIα-D308A (D), AP-3-binding-deficient mutant PI4KIIα-L61,62A (E) or PI4KIIβ-WT (F) and selected for at least two weeks to allow for stable expression of the GFP-tagged protein. Cells were then transduced with lentiviruses expressing control non-coding shRNA (shNC) or shPI4KIIα-1. **(*A-F*)** 7 to 14 d after shRNA transduction, cells were analyzed by IFM for GFP-tagged protein (white; left panels) and endogenous TYRP1 (green; middle left and merged right panels) and by bright field

microscopy for pigment granules (BF; middle right panels and pseudocolored magenta in the merged images on the right). White arrows, examples of TYRP1 surrounding pigment granules; yellow arrowheads, examples of mislocalized TYRP1 relative to pigment granules. Boxed regions are magnified 5-fold in the insets. Scale bars: main panels, 10 μm; insets, 2 μm. **(*G*)** Quantification of the degree to which TYRP1 overlapped melanosomes in cells treated with the indicated shRNAs either alone or expressing exogenous GFP-tagged protein. Data are presented as a scatter plot in which individual cells are indicated by single dot colored to represent one of at least three independent experiments; means of each experiment are indicated by triangles, and the overall mean and SD are indicated by bars. Datasets were analyzed by Welch's ANOVA test; ****, $p<0.0001$; NS, not significant. **(*H*)** Whole-cell lysates from cells in A-E were analyzed by SDS/PAGE and immunoblotting for PI4KIIα and γ-Tubulin as a loading control; positions of molecular weight markers (MW) are indicated to the left. Immunoblotting for PI4KIIβ in cells (F) is shown in Figure 4.

Figure 4. PI4KIIβ function in TYRP1 trafficking requires its lipid kinase activity and binding to adaptor AP-1.

WT melan-Ink4a were untransduced (A, B) or transduced with retroviruses encoding hygromycin resistance and GFP-tagged PI4KIIβ-WT (C), kinase-dead mutant PI4KIIβ-D304A (D), AP-1-binding-deficient mutant PI4KIIβ-L29,30A (E) or PI4KIIα-WT (F) and selected for at least two weeks to allow for stable expression of the GFP-tagged protein. Cells were then transduced with lentiviruses expressing control non-coding shRNA (shNC) or shPI4KIIβ-2 shRNA to PI4KIIβ. **(*A-F*)** 7 to 14 d after shRNA transduction, cells were analyzed by IFM for the GFP-tagged protein (white; left panels) and for endogenous TYRP1 (green; middle left panels and merged panels at right) and by bright field microscopy for pigment granules (BF; middle right panels and pseudocolored magenta in the merged images on the right). White arrows, examples of TYRP1

surrounding pigment granules; yellow arrowheads, examples of TYRP1 puncta that do not overlap with pigment granules. Boxed regions are magnified 5-fold in the insets. Scale bars: main panels, 10 μm; insets, 2 μm. **(*G*)** Quantification of the degree to which TYRP1 overlaps pigment granules in cells treated with the indicated shRNAs either alone or expressing exogenous GFP-tagged protein. Data are presented as a scatter plot in which individual cells are indicated by a single dot colored to represent one of at least three independent experiments; means of each experiment are indicated by triangles, and the overall mean and SD are indicated by bars. Datasets were analyzed by Welch's ANOVA test; ****, $p<0.0001$; NS, not significant. **(*H*)** Whole-cell lysates from cells in A-E were analyzed by SDS/PAGE and immunoblotting for PI4KIIβ and γ-Tubulin as a loading control. **(*I*)** Whole-cell lysates from cells in panel F and Fig. 3F were analyzed by SDS/PAGE and immunoblotting for PI4KIIα, PI4KIIβ and γ-Tubulin. Positions of molecular weight markers (MW) are indicated to the left in H and I.

Figure 5. Type II PtdIns4-kinases are required after BLOC-1 function in tubular transport to melanosomes.

BLOC-1$^{-/-}$ melan-pa melanocytes from *pallid* mice (A and B) or WT melan-Ink4a melanocytes (C and D) were transduced with lentiviruses expressing the indicated shRNAs to PI4KIIα, PI4KIIβ or control non-coding shRNA (shNC) for 7 to 14 d. **(*A*)** After transduction**,** BLOC-1$^{-/-}$ melanocytes were analyzed by IFM for endogenous TYRP1 (green; left and right panels), TfR to mark early endosomes (magenta, middle and right panels), and either PI4KIIα or PI4KIIβ (not shown) to indicate knock down efficiency. Only cells with minimal PI4KIIα or PI4KIIβ signal are shown. Yellow arrowheads, examples of TYRP1 overlap with TfR. Boxed regions are magnified 5-fold in the insets. Scale bars: main panels, 10 μm; insets, 2 μm. (***B***) Quantification of the degree to which TYRP1 overlapped TfR in cells treated with the indicated shRNAs. Data are presented as a scatter plot in which individual cells are indicated by single dot colored to represent one of two independent experiments; means of each experiment are indicated by triangles, and overall mean

and SD are indicated by bars. Datasets were analyzed by ordinary one-way ANOVA test. **(*C*, *D*)** WT melan-Ink4a melanocytes treated with the indicated shRNAs were homogenized and fractionated to yield postnuclear membrane (M) and cytosolic (C) fractions (see *Materials and Methods*). Identical cell equivalents of membrane and cytosolic fractions were fractionated by SDS-PAGE and analyzed by immunoblotting using antibodies to the indicated subunits of BLOC-1, AP-1, and AP-3. **(*C*)** Representative blots. Positions of molecular weight (MW) markers are indicated at left. **(*D*)** Quantification of the percentage of each protein that was associated with the membrane fraction relative to the total cellular content in panel C. Data are presented as mean ± SD of 4 independent experiments and analyzed by ordinary one-way ANOVA test. NS, not significant.

Figure 6. Type II PtdIns4-kinases and PtdIns4P are present on endosomal tubular carriers

(*A-C*) WT Melan-Ink4a melanocytes stably expressing mCherry-STX13 (magenta, middle and right panels) were transiently transfected with GFP-tagged PI4KIIα (A), PI4KIIβ (B) or P4C-SidC (C; green, left and right panels) and then analyzed by dual-view live cell-spinning disc microscopy. Shown are the individual labels and merged image from a frame of a representative cell emphasizing tubular structures; two boxed regions are magnified 5-fold in the insets. Yellow arrowheads, examples of tubular structures positive for both mCherry-STX13 and either PI4KIIα-GFP, PI4KIIβ-GFP, or GFP-P4C-SidC. Scale bars: main panels, 10 μm; insets, 2 μm.

Figure 7. PI4KIIα and PI4KIIβ associate with tubules with distinct kinetics and together generate PtdIns4P throughout the lifetime of the tubule.

As in **Fig. 6**, WT Melan-Ink4a melanocytes stably expressing mCherry-STX13 were transiently transfected with GFP-tagged PI4KIIα (A), PI4KIIβ (B) or P4C-SidC (C) and then analyzed by dual-

view live-cell spinning-disk microscopy. Shown are a montage of individual and merged image sequences from the indicated insets from **Fig. 6** emphasizing the successive extension of STX13-containing tubules from a source endosome. White arrowheads, sources of tubules; yellow arrowheads, tips of tubules; time from onset of tubule formation is indicated in seconds. As in A, GFP-PI4KIIα was present on nascent tubules in 22 out of 24 instances in which the source endosome and a nascent tubule were visible and distinguishable in the same plane of focus (n=6 cells, 3 independent experiments). As in B, GFP- PI4KIIβ joined pre-formed tubules in 20 out of 26 instances in which the source endosome and a nascent tubule were visible and distinguishable in the same plane of focus (n=9 cells, 3 independent experiments). Scale bars: 2 μm.

Figure 8. PI4KIIα and PI4KIIβ are both required to maintain PtdIns4P on endosomal tubules. WT melan-Ink4a melanocytes stably expressing GFP-P4C-SidC (P4C) were transduced with lentiviruses encoding control shRNA (shNC) or the indicated shRNAs to PI4KIIα or PI4KIIβ, selected for 7 to 14 d, and then transiently transfected with mCherry-STX13 (STX13) and analyzed by live-cell spinning-disk microscopy. **(*A*)** Still images from image streams of cells treated with shNC (Aa-c) shPI4KIIα (Ad-f) or shPI4KIIβ (Ag-i) showing P4C (green, left panels), STX13 (magenta, middle panels), and their overlap (merged images on the right). Yellow arrowheads, STX13-containing tubules that overlap with P4C; white arrowheads, STX13-containing tubules that do not overlap with P4C. Boxed regions are magnified 5-fold in the insets. Scale bars: main panels, 10 μm; insets, 2 μm. **(*B*, *C*)** The total numbers of either single P4C-positive (B) or double P4C- and STX13-positive tubules per 100-μm^2 area in each cell population was quantified as described in *Materials and Methods*. **(*D*)** The percentage of all tubules that were double positive for P4C and STX13 was calculated for each cell population. All data in B-D are presented as scatter plots in which each dot represents a cell color coded to each of three independent experiments and colored triangles represent means from each independent

experiment; the overall mean ± SD are indicated by bars. Data were analyzed by either Kruskal-Wallis (A) or ordinary one-way ANOVA test (B, C). **(*E*)** Fractions of cells with indicated percentage of double P4C- and STX13-positive tubules in each shRNA-treated population was quantified. Data are presented as mean ± SD of 3 independent experiments and analyzed by Kruskal-Wallis test. ****, $p<0.0001$; *, $p<0.05$; NS, not significant.

Figure 9. Depletion of either PI4KIIα or PI4KIIβ disrupts the dynamics of BLOC-1-dependent tubular cargo carriers.

A-G. WT melan-Ink4a melanocytes stably expressing mCherry-STX13 (mCh-STX13) were transduced with lentiviruses expressing control shRNA (shNC) or the indicated shRNAs to PI4KIIα or PI4KIIβ, selected for 7 to 14 d, and then analyzed by live cell-spinning disc microscopy. **(*A-C*)** Still images from image streams (a panels; boxed regions are magnified 4-fold in insets in b panels), and skeletonized images (c, d) documenting the appearance of tubules. Scale bars: main panels, 12 μm; insets, 3 μm. **(*D*)** The total number of mCh-STX13-labeled tubules per 25-μm^2 area in each cell population was quantified as described in *Materials and Methods*. **(*E*)** The total number of tubules per 25-μm^2 area that were longer than 1 μm was quantified for each cell population. **(*F*)** The percentage of total tubules (D) that were longer than 1 μm (E) was calculated for each cell population. **(G)** The length of all tubules per 25-μm^2 area was quantified for each cell population. All data in D-G are presented as scatter plots in which each dot is a cell color coded to each of three independent experiments; means from each independent experiment are indicated by colored triangles. Overall mean ± SD is indicated by bars. Data were analyzed by either Kruskal-Wallis (D) or ordinary one-way ANOVA test (E, F). (****, $p<0.0001$; ***, $p<0.001$; *, $p<0.05$; NS, not significant). **(*H*)** Working model shows that PI4KIIα (pink and green) is recruited by AP-3 (blue) on the vacuolar endosome to newly forming endosomal tubules labeled by STX13 through the interaction of AP-3, BLOC-1 (orange), and PI4KIIα (top panel). As the tubule

elongates, PI4KIIβ (blue and green) is recruited by AP-1 (green) – perhaps bound to the kinesin motor heavy chain KIF13A (red) – to the extended tubule (bottom panel). Both PI4KIIα and PI4KIIβ generate local PtdIns4P (yellow shading) to allow for effective transport of cargos (TYRP1, OCA2 and VAMP7 as indicated) to melanosomes.

Figure 1

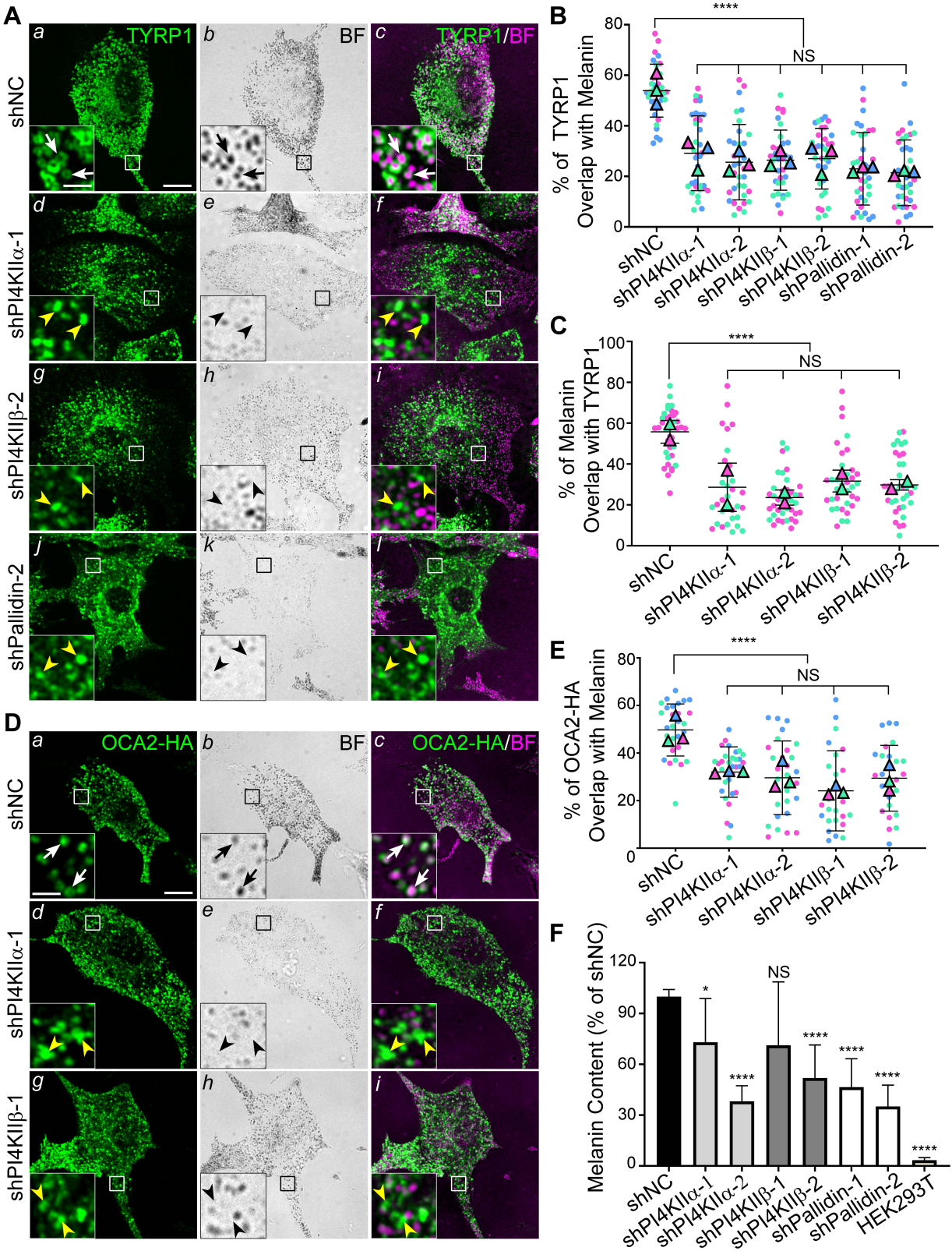
A
a TYRP1
b BF
c TYRP1/BF
shNC
d
e
f
shPI4KIIα-1
g
h
i
shPI4KIIβ-2
j
k
l
shPallidin-2
B
% of TYRP1 Overlap with Melanin
****
NS
shNC
shPI4KIIα-1
shPI4KIIα-2
shPI4KIIβ-1
shPI4KIIβ-2
shPallidin-1
shPallidin-2
C
% of Melanin Overlap with TYRP1
D
a OCA2-HA
b BF
c OCA2-HA/BF
shNC
d
e
f
shPI4KIIα-1
g
h
i
shPI4KIIβ-1
E
% of OCA2-HA Overlap with Melanin
F
Melanin Content (% of shNC)
*
HEK293T

Figure 2

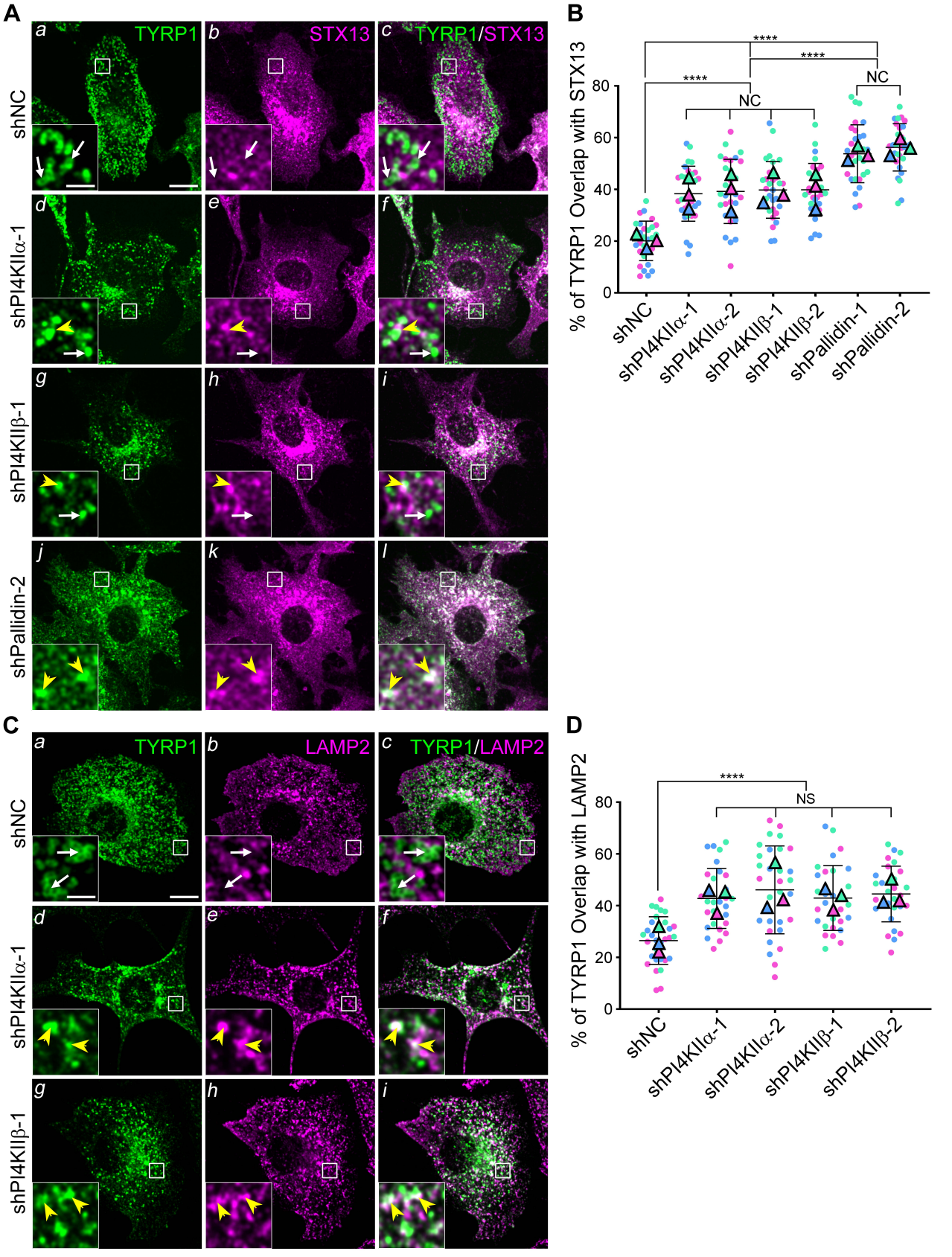
A
a TYRP1
b STX13
c TYRP1/STX13
shNC
d
e
f
shPI4KIIα-1
g
h
i
shPI4KIIβ-1
j
k
l
shPallidin-2
B
% of TYRP1 Overlap with STX13
0
20
40
60
80
****
****
****
NC
NC
shNC
shPI4KIIα-1
shPI4KIIα-2
shPI4KIIβ-1
shPI4KIIβ-2
shPallidin-1
shPallidin-2
C
a TYRP1
b LAMP2
c TYRP1/LAMP2
shNC
d
e
f
shPI4KIIα-1
g
h
i
shPI4KIIβ-1
D
% of TYRP1 Overlap with LAMP2
0
20
40
60
80
****
NS
shNC
shPI4KIIα-1
shPI4KIIα-2
shPI4KIIβ-1
shPI4KIIβ-2

Figure 3

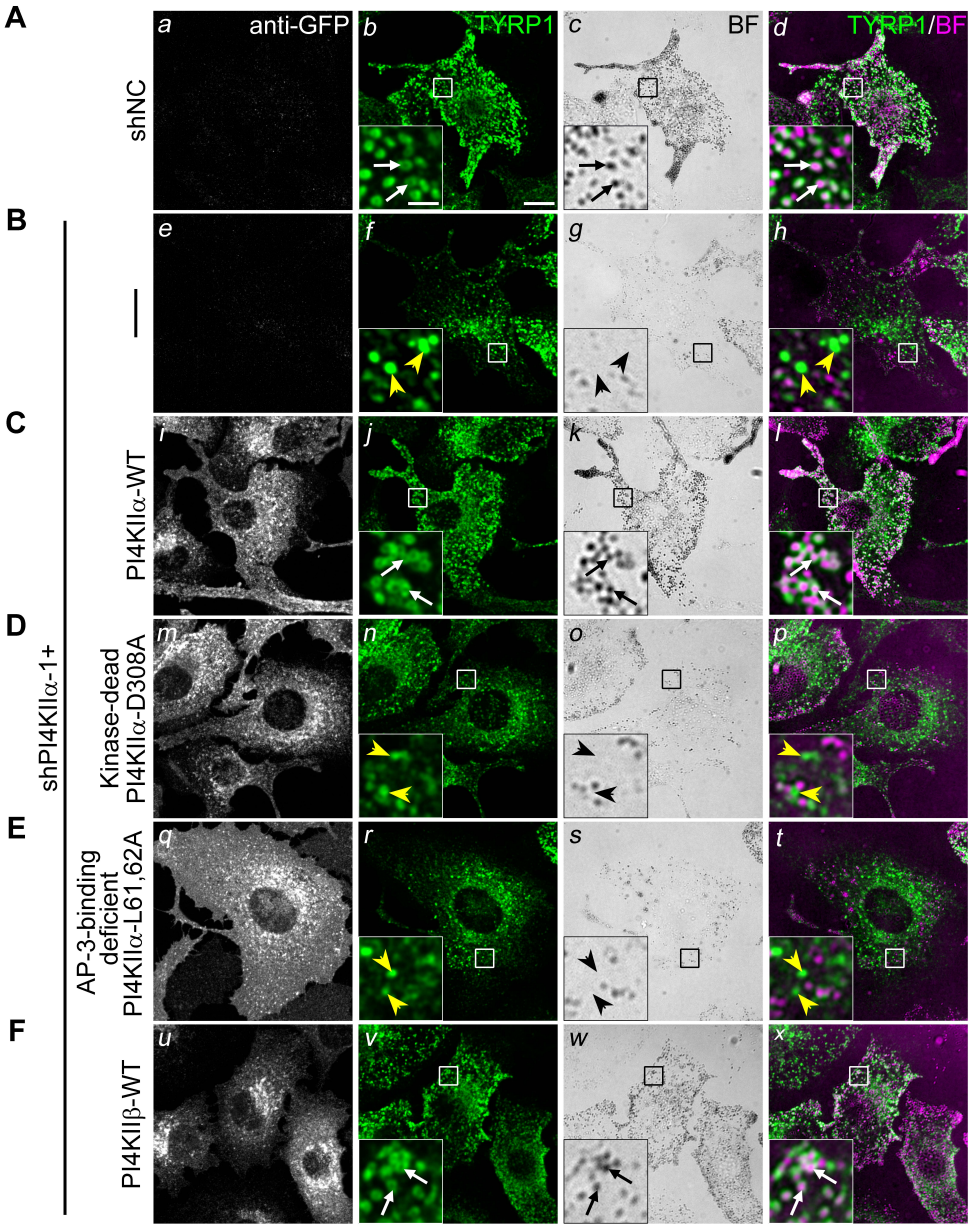
A
B
C
D
E
F
a
anti-GFP
b
TYRP1
c
BF
d
TYRP1/BF
shNC
e
f
g
h
—
i
j
k
l
PI4KIIα-WT
m
n
o
p
Kinase-dead PI4KIIα-D308A
q
r
s
t
AP-3-binding deficient PI4KIIα-L61,62A
u
v
w
x
PI4KIIβ-WT
shPI4KIIα-1+

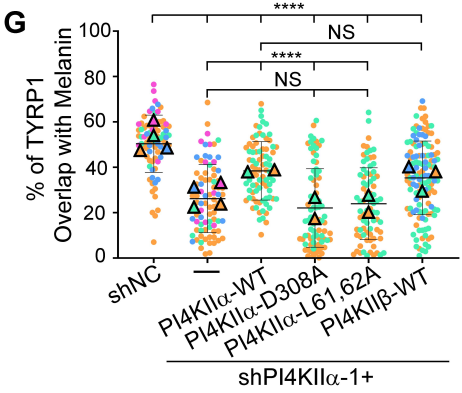
G
% of TYRP1 Overlap with Melanin
100
80
60
40
20
0
****
NS
****
NS
shNC
—
PI4KIIα-WT
PI4KIIα-D308A
PI4KIIα-L61,62A
PI4KIIβ-WT
shPI4KIIα-1+

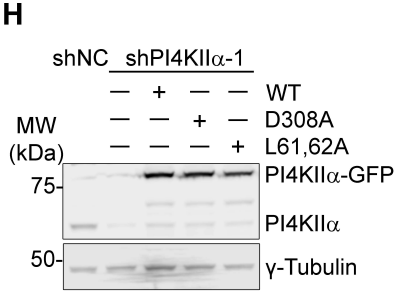
H
shNC
shPI4KIIα-1
WT
D308A
L61,62A
MW (kDa)
75-
50-
PI4KIIα-GFP
PI4KIIα
γ-Tubulin

Figure 4

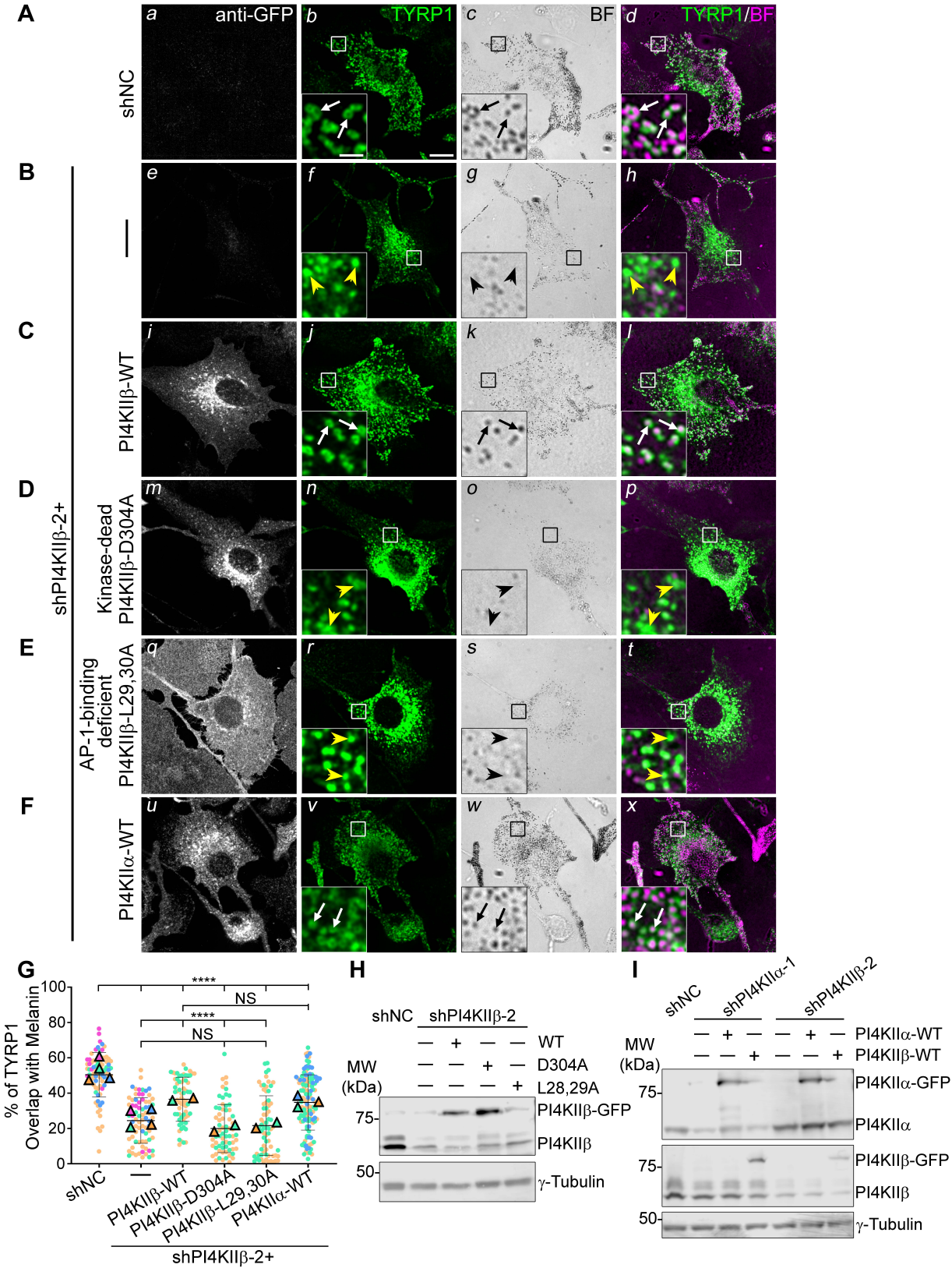
A
B
C
D
E
F
G
H
I
a anti-GFP
b TYRP1
c BF
d TYRP1/BF
shNC
e
f
g
h
—
i
j
k
l
PI4KIIβ-WT
m
n
o
p
Kinase-dead PI4KIIβ-D304A
q
r
s
t
AP-1-binding deficient PI4KIIβ-L29,30A
u
v
w
x
PI4KIIα-WT
shPI4KIIβ-2+
% of TYRP1 Overlap with Melanin
100
80
60
40
20
0
****
NS
****
NS
shNC
—
PI4KIIβ-WT
PI4KIIβ-D304A
PI4KIIβ-L29,30A
PI4KIIα-WT
shPI4KIIβ-2+
shNC
shPI4KIIβ-2
WT
D304A
L28,29A
MW (kDa)
75
50
PI4KIIβ-GFP
PI4KIIβ
γ-Tubulin
shNC
shPI4KIIα-1
shPI4KIIβ-2
PI4KIIα-WT
PI4KIIβ-WT
MW (kDa)
75
PI4KIIα-GFP
PI4KIIα
75
PI4KIIβ-GFP
PI4KIIβ
50
γ-Tubulin

Figure 5

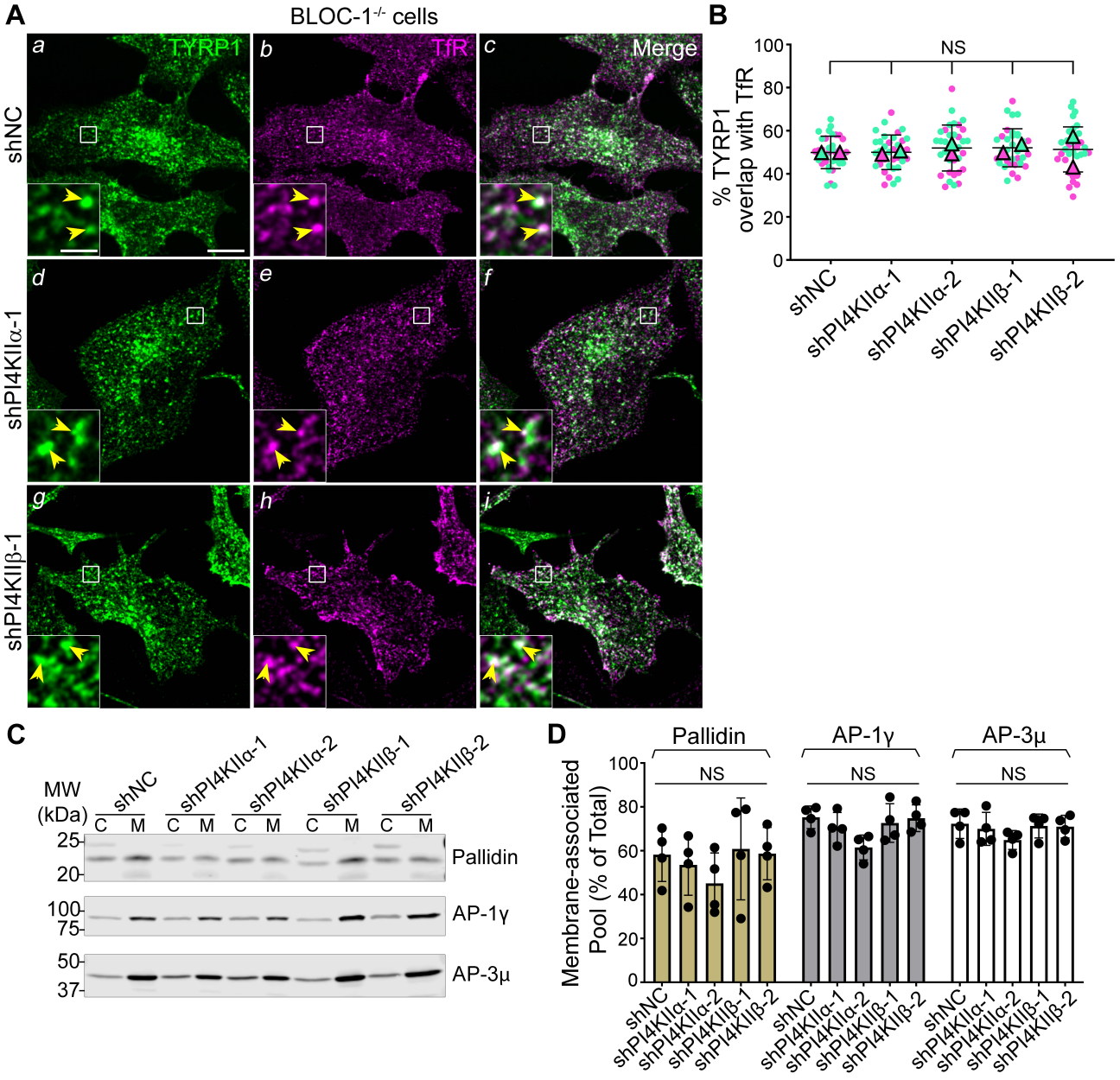
A
BLOC-1-/- cells
TYRP1
TfR
Merge
shNC
shPI4KIIα-1
shPI4KIIβ-1
B
% TYRP1 overlap with TfR
NS
shNC
shPI4KIIα-1
shPI4KIIα-2
shPI4KIIβ-1
shPI4KIIβ-2
C
MW (kDa)
Pallidin
AP-1γ
AP-3μ
D
Membrane-associated Pool (% of Total)
Pallidin
AP-1γ
AP-3μ
NS

Figure 6

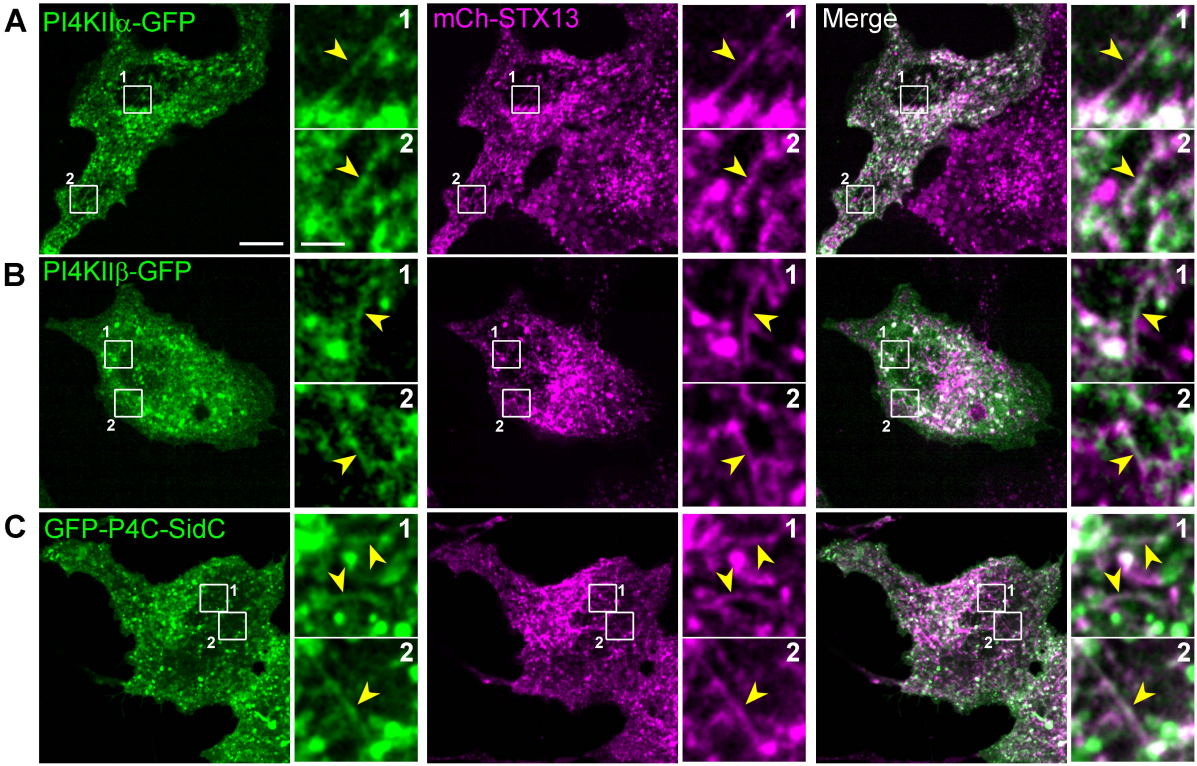

Figure 7

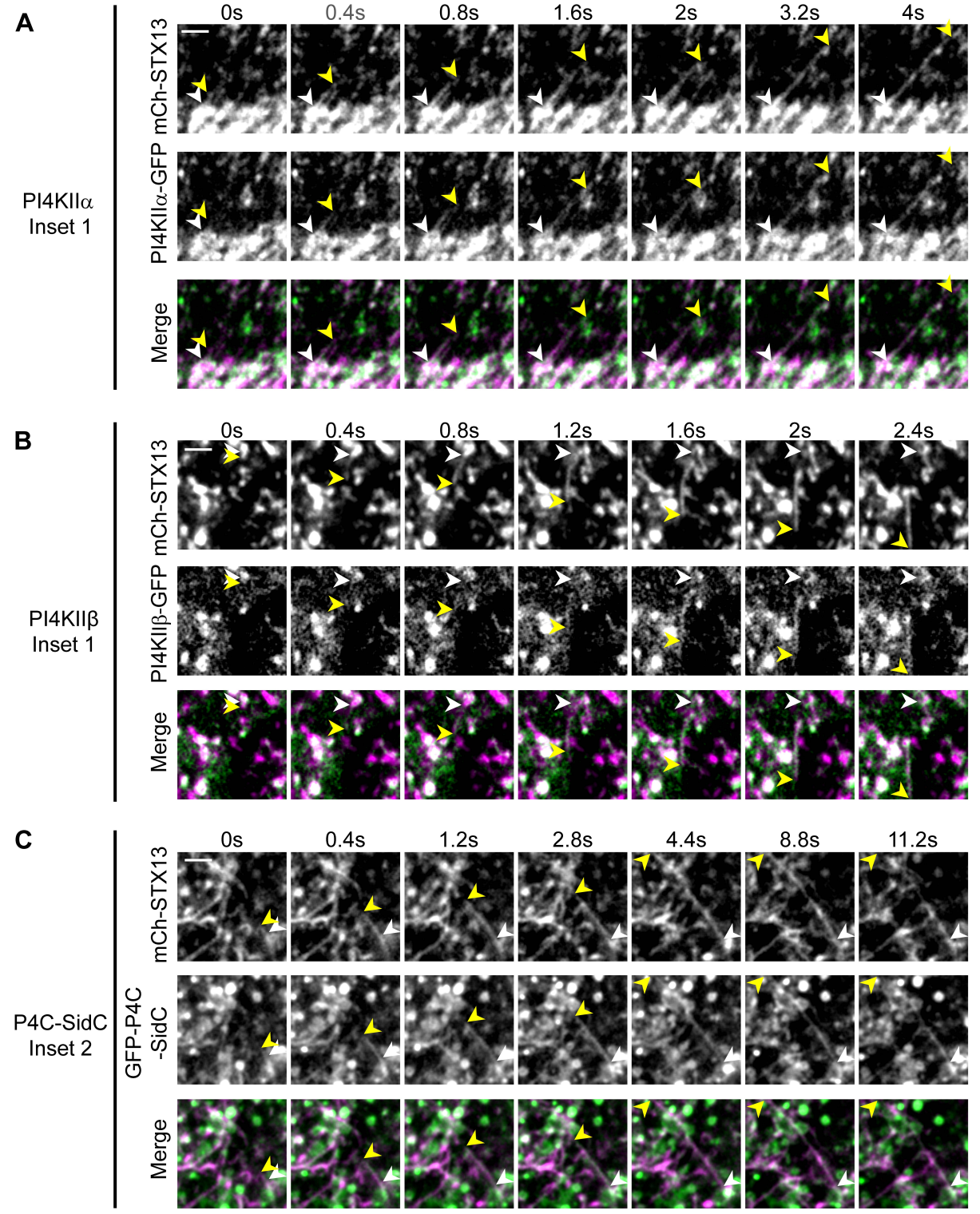
A
0s
0.4s
0.8s
1.6s
2s
3.2s
4s
mCh-STX13
PI4KIIα-GFP
Merge
PI4KIIα
Inset 1
B
0s
0.4s
0.8s
1.2s
1.6s
2s
2.4s
mCh-STX13
PI4KIIβ-GFP
Merge
PI4KIIβ
Inset 1
C
0s
0.4s
1.2s
2.8s
4.4s
8.8s
11.2s
mCh-STX13
GFP-P4C
-SidC
Merge
P4C-SidC
Inset 2

Figure 8

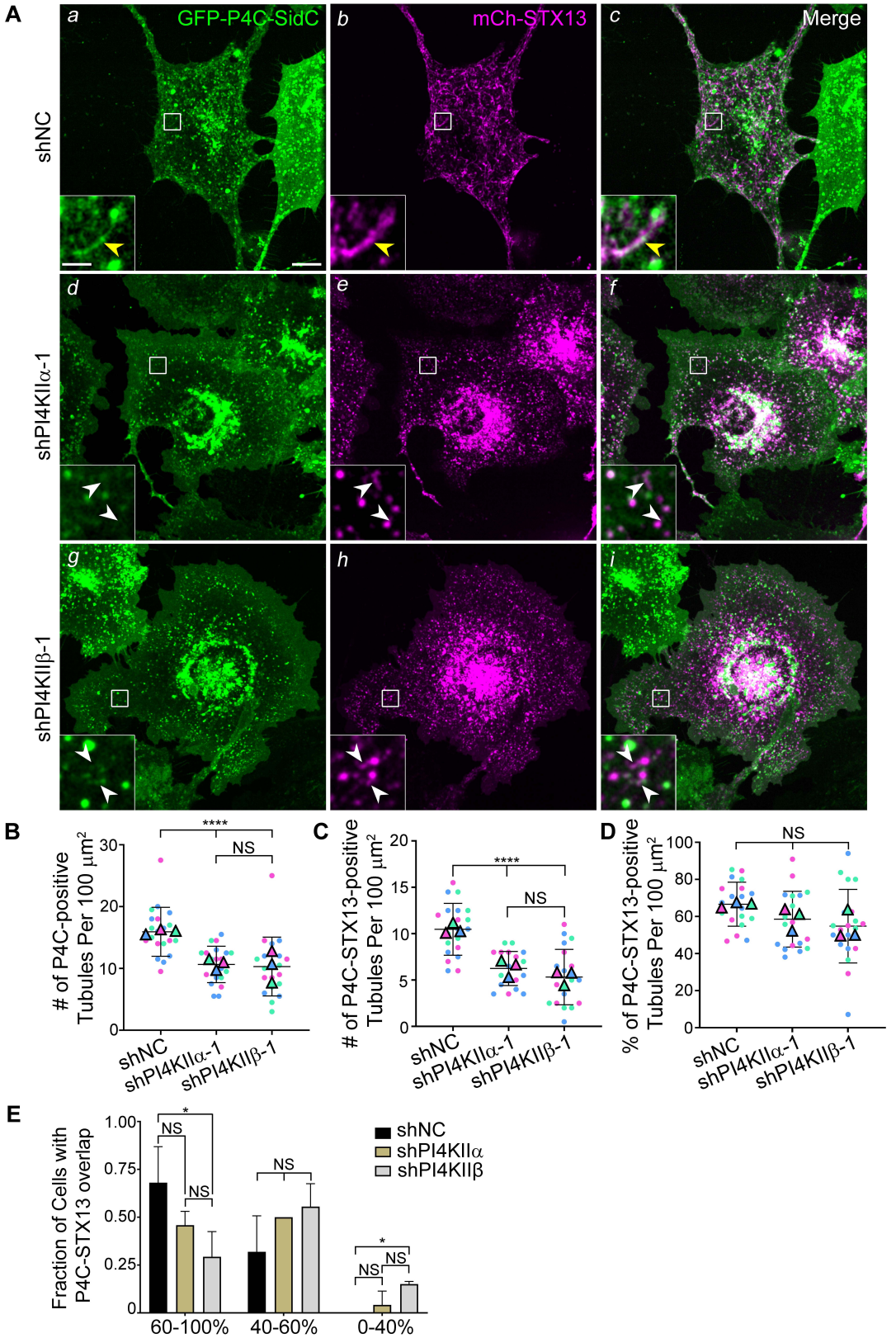
A
a
GFP-P4C-SidC
b
mCh-STX13
c
Merge
shNC
d
e
f
shPI4KIIα-1
g
h
i
shPI4KIIβ-1
B
# of P4C-positive Tubules Per 100 μm²
****
NS
shNC
shPI4KIIα-1
shPI4KIIβ-1
C
# of P4C-STX13-positive Tubules Per 100 μm²
****
NS
D
% of P4C-STX13-positive Tubules Per 100 μm²
NS
E
Fraction of Cells with P4C-STX13 overlap
shNC
shPI4KIIα
shPI4KIIβ
60-100%
40-60%
0-40%
*
NS

Figure 9

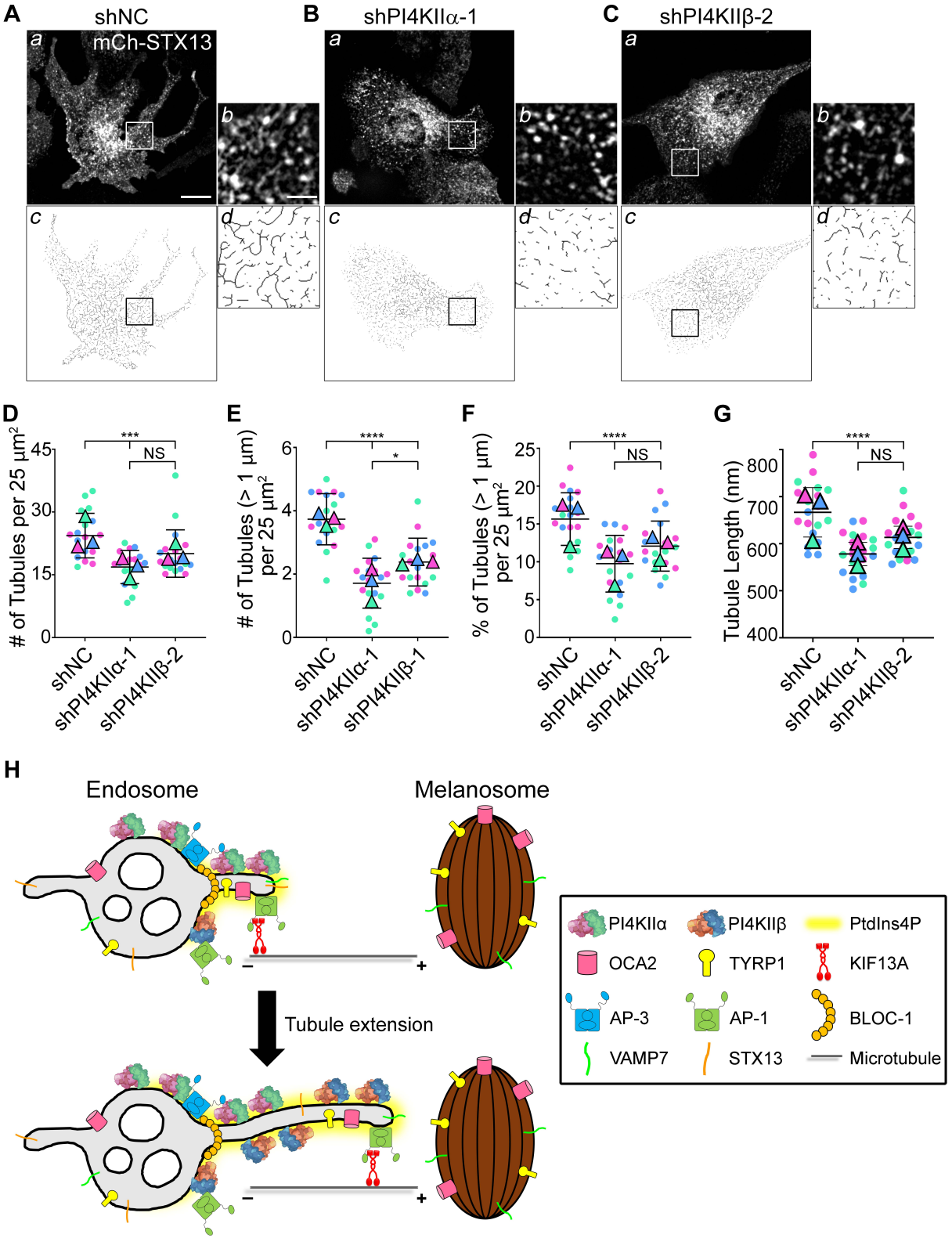
A
shNC
mCh-STX13
B
shPI4KIIα-1
C
shPI4KIIβ-2
a
b
c
d
D
# of Tubules per 25 μm²
***
NS
shNC
shPI4KIIα-1
shPI4KIIβ-2
E
# of Tubules (> 1 μm) per 25 μm²
****
*
shNC
shPI4KIIα-1
shPI4KIIβ-1
F
% of Tubules (> 1 μm) per 25 μm²
****
NS
shNC
shPI4KIIα-1
shPI4KIIβ-2
G
Tubule Length (nm)
****
NS
shNC
shPI4KIIα-1
shPI4KIIβ-2
H
Endosome
Melanosome
Tubule extension
PI4KIIα
PI4KIIβ
PtdIns4P
OCA2
TYRP1
KIF13A
AP-3
AP-1
BLOC-1
VAMP7
STX13
Microtubule